CHALMERS

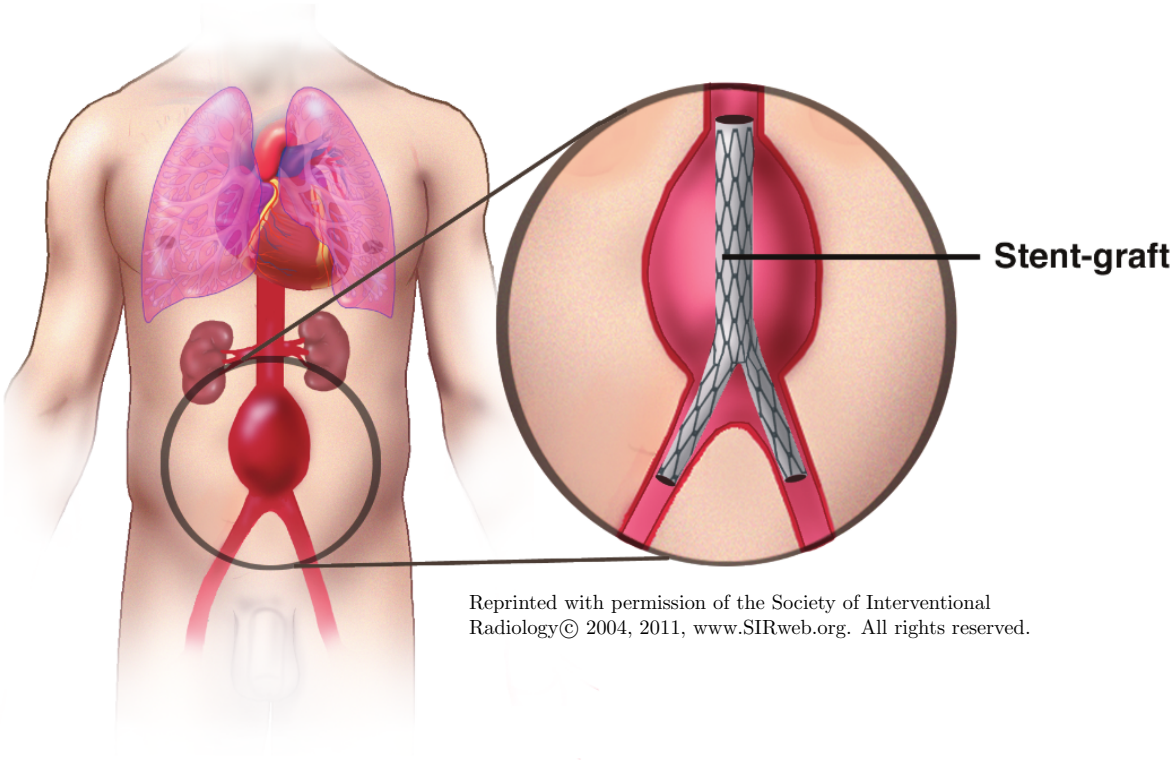

Fluid-Structure Interaction analysis of the forces causing stent graft migration

Master's Thesis in Solid and Fluid Mechanics

PATRIK ANDERSSON
JOHAN PILQVIST

Department of Applied Mechanics
Division of Material & Computational Mechanics and Division of Fluid Mechanics
CHALMERS UNIVERSITY OF TECHNOLOGY
Göteborg, Sweden 2011
Master's Thesis 2011:23

MASTER'S THESIS 2011:23

Fluid-Structure Interaction analysis of the forces causing stent graft migration

Master's Thesis in Solid and Fluid Mechanics

PATRIK ANDERSSON
JOHAN PILQVIST

Department of Applied Mechanics
Division of Material & Computational Mechanics and Division of Fluid Mechanics
CHALMERS UNIVERSITY OF TECHNOLOGY

Göteborg, Sweden 2011

Fluid-Structure Interaction analysis of the forces causing stent graft migration
PATRIK ANDERSSON
JOHAN PILQVIST

Master's Thesis 2011:23
ISSN 1652-8557
Department of Applied Mechanics
Division of Material & Computational Mechanics and Division of Fluid Mechanics
Chalmers University of Technology
SE-412 96 Göteborg
Sweden
Telephone: + 46 (0)31-772 1000

Cover:
Abdominal aortic aneurysm reinforced by a stent graft.

Chalmers Reproservice
Göteborg, Sweden 2011

Fluid-Structure Interaction analysis of the forces causing stent graft migration
Master's Thesis in Solid and Fluid Mechanics
PATRIK ANDERSSON
JOHAN PILQVIST
Department of Applied Mechanics
Division of Material & Computational Mechanics and Division of Fluid Mechanics
Chalmers University of Technology

Abstract

Abdominal aortic aneurysm, a disorder involving a local dilatation of the abdominal aortic vessel, is a disease common among males in their late sixties and a major cause of death in case of rupture. An aneurysm can be treated with major open surgery or with minimally invasive techniques. One such treatment, called Endovascular Aortic Repair (or EVAR), is the insertion of stent grafts redirecting the blood flow through a bifurcating tube consisting of a special fabric supported by a reinforcing metallic mesh. This procedure is preferrable in the sense that it does not require an open surgery. However, there are some problems arising from the fact that the stent graft is not fixated at its lower extremities. When subjected to a pulsating blood flow the bifurcating portions of stent graft may thus experience detachment from the vessel walls (commonly referred to as stent graft migration), leading to fatal blood leakage. The forces causing such detachments are therefore of great interest.

The development of numerical methods for Fluid-Structure Interaction (FSI) analyses provides possibilities to study the flow through a stent graft and the forces it exerts on the attachment regions. This report presents the results from FSI simulations using the two softwares LS-DYNA and OpenFOAM. The scenarios studied in this work include a steady flow of water and a sinusoidal flow of water through a bent, flexible tube resembling one of the lower extremities of a stent graft. The different softwares utilize different numerical approaches to formulate the FSI problem. LS-DYNA uses a Finite Element (FE) based Arbitrary Lagrangian-Eulerian (ALE) formulation, while OpenFOAM uses the Finite Volume (FV) method. In addition to the flow analysis and extraction of the forces, the use of the different softwares allows for a comparison between the two numerical approaches.

For both scenarios, the flow characteristics in the different softwares show fair correspondence and the extracted forces are of the same orders of magnitude. However, some previous studies, such as the work performed by Li and Kleinstreuer [1], point towards larger forces than those extracted in this work. These differenes are likely to originate from the differences in geometries, material properties and boundary conditions. Nonetheless, the results show good promise for continuation of similar studies in the future.

Keywords: Abdominal Aortic Aneurysm, Stent Graft, FSI, OpenFOAM, LS-DYNA

Preface

This Master's Thesis project is carried out at the department of Applied Mechanics as a part of the Solid and Fluid Mechanics Master's progamme at Chalmers University of Technology in Göteborg, Sweden, during a period of twenty weeks in the spring of 2011. The work is cross-divisional involving tutors from both the division of Material & Computational Mechanics and the division of Fluid Mechanics. This report presents the results from multiple computational Fluid-Structure Interaction (FSI) analyses conducted on a flexible stent graft model. Both a scenario simulating a steady water flow and another scenario simulating a sinusoidal water flow through the stent graft are performed.

Acknowledgements

The authors would like to thank the tutors, Professor Ragnar Larsson (division of Material & Computational Mechanics) and Associate Professor Håkan Nilsson (division of Fluid Mechanics), for their guidance and support throughout the project. We would also like to thank post-graduate Karin Brolin, PhD Per-Anders Eggertsen and the support team at Engineering Resources AB for their help with LS-DYNA. Further thanks to MD Håkan Roos at Sahlgrenska University Hospital for being a source of both information and inspiration and Professor Hrvoje Jasak for providing the solver used in the OpenFOAM simulations. The Swedish National Infrastructure for Computing (SNIC) is acknowledged for providing computational resources. Last, but not least, we would like to extend our gratitude to Jesper Lindberg for providing a python script enabling the mesh conversion from ANSYS ICEM CFD to LS-DYNA.

Göteborg June 2011
Patrik Andersson, Johan Pilqvist

Nomenclature

α_i^e	Volume fraction in element e of material i [-]
a	Acceleration [m/s^2]
$\mathbf{b}$	Vectorial body force [N/kg]
$\tilde{B}$	Referential domain [-]
B	Spatial domain [-]
B_0	Material domain [-]
d	Contact penetration depth [m]
η	Poisson's ratio [-]
$\mathbf{E}$	Green-Lagrangian strain tensor [-]
$\boldsymbol{\varphi}$	Material map [-]
$\boldsymbol{\varphi}^*$	Particle map [-]
$\tilde{\boldsymbol{\varphi}}$	Mesh map [-]
$\mathbf{F}_{contact}$	Contact force between fluid and solid nodes [N]
f	Control volume face [-]
h	Thickness [m]
K	Bulk modulus [Pa]
k_d	Damping coefficient [N·s/m]
k_s	Stiffness coefficient [N/m]
μ	Dynamic viscosity [N·s/m^2]
$\mathbf{n}_f$	Control volume face unit normal [-]
∇	Vector gradient operator [-]
$\nabla_{\mathbf{X}}$	Material gradient operator [-]
ν	Kinematic viscosity [m^2/s]
ω	Angular velocity [rad/s]
$\boldsymbol{\mathcal{P}}$	1$^{\text{st}}$ Piola-Kirchhoff stress tensor [N/m^2]
p	Pressure [Pa]
ρ	Continuum density [kg/m^3]
r_f	Radius of fluid particle [m]
r_s	Radius of solid particle [m]

$\boldsymbol{\Sigma}$ 2^{nd} Piola-Kirchhoff stress tensor [N/m^2]

S_f Control volume face area [m^2]

$\boldsymbol{\tau}$ Viscous stress tensor [N/m^2]

$\mathbf{t}$ Vectorial force per unit surface area (traction) [N/m^2]

$\mathbf{u}$ Vectorial displacement [m]

$\mathbf{v}$ Vectorial velocity [m/s]

v_{sound} Speed of sound [m/s]

w_{pc} Interpolation weighting factor [-]

$\tilde{\mathbf{X}}$ Referential coordinate [m]

$\mathbf{X}$ Material coordinate [m]

$\mathbf{x}$ Spatial coordinate [m]

ζ Arbitrary function [-]

Acronyms

ALE Arbitrary Lagrangian-Eulerian. Page 2

CFL Courant-Friedrichs-Lewy. Page 16

CV Control volume. Page 6

EVAR Endovascular Aortic Repair. Page 1

EVG Endovascular Graft. Page 4

FE Finite Element. Page 2

FSI Fluid-Structure Interaction. Page 2

FV Finite Volume. Page 2

HIS Half Index Shift. Page 16

LD LS-DYNA. Page 2

MMALE Multi Material ALE. Page 8

MUSCL Monotone Upwind Schemes for Conservation Laws. Page 16

OF OpenFOAM. Page 2

PISO Pressure-Implicit Split-Operator. Page 16

Contents

1 Introduction

Abdominal aortic aneurysm is a localized dilatation of the abdominal aortic vessel and is a disorder common for males of 65 years of age and older. The aneurysm, or dilatation of the aorta, increases the tension (and hence yields a weakening) of the vessel wall, according to the law of Laplace [2]. This significantly increases the risk of rupture on the aorta which, if remained untreated, is highly lethal. To prevent rupture, aneurysms are generally treated with a prophylactic operation. The classical treatment of abdominal aortic aneurysm consists of a major open operation, where the aim is to replace the affected vessel wall with a prosthesis, i.e. a tube consisting of Dacron or e-PTFE (gore-tex) as shown in Figure 1.1a. Such tubes are called grafts. An alternative treatment, which is well established and used in practice worldwide, is to adopt an internal reinforcement of the aneurysm, relining the vessel using so-called stent grafts. The stent grafts are inserted percutaneously[1] using x-ray technique, and consists of a special fabric supported by a metallic mesh covered by a skin, see Figure 1.1b and Figure 1.2. This treatment is named Endovascular Aortic Repair (EVAR).

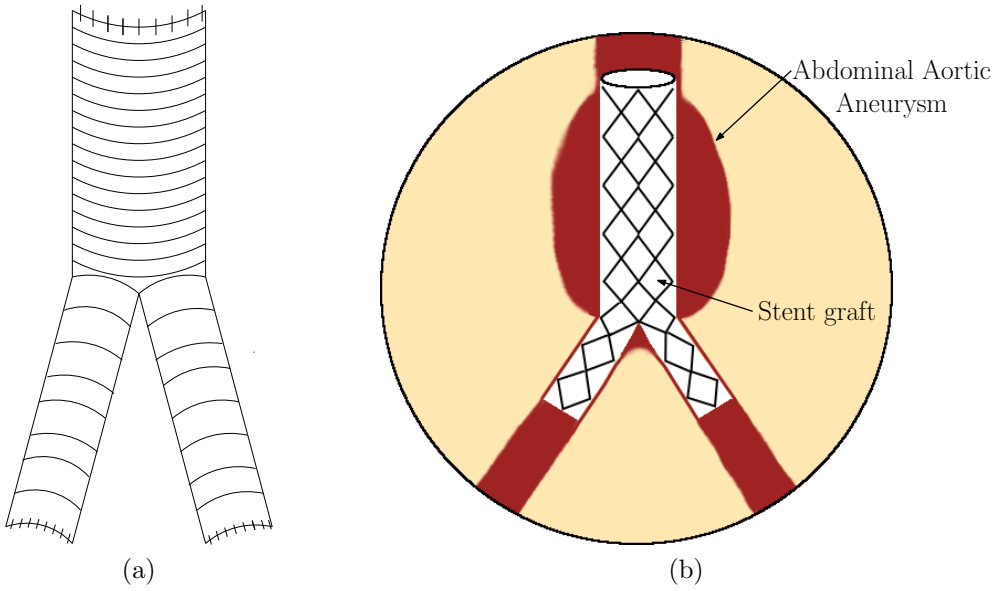

Figure 1.1: a) Schematic illustration of a dacron tube used in open surgery and b) a reinforced aneurysm using a stent graft (EVAR treatment).

1.1 Problem description

The method of using stent grafts as a treatment involves some difficulties regarding attachment of the reinforcing structure. As opposed to an open surgery procedure, where the structure is stitched together with the blood vessel at all extremeties, the standard procedure is to anchor hooks at the upper attachment point of the stent graft, while the lower bifurcating extensions are kept in place only by self expansion against the vessel walls (see Figure 1.2). The fact that the bifurcating portions of the stent graft are not fixated gives rise to a risk of detachment when subjected to a pulsating blood flow. Such a detachment is often referred to as stent graft migration, consequently leading to a pressurized blood flow in the aneurysm which increases the risk of rupture.

[1] i.e. by piercing the skin with a needle catheter, followed by insertion of a wire through the needle pathway.

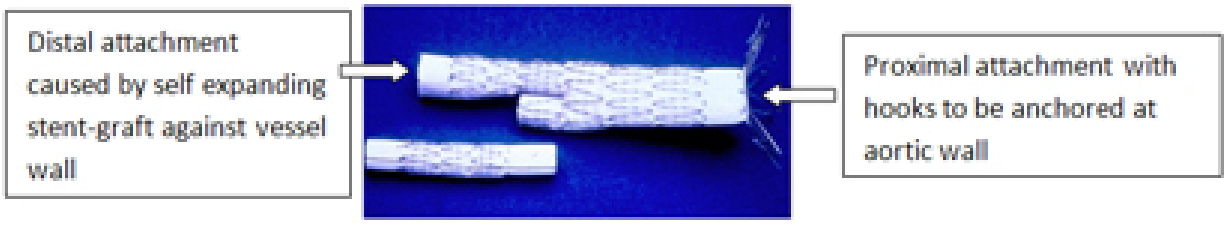

Figure 1.2: Stent graft used in EVAR with distal attachment.

1.2 Purpose

In 1999 Resch et al. [3] reported that 26 out of 58 patients (45%) showed distal migration of stent grafts during a mean follow-up time of thirteen months. Four years later, Zarins et al. [4] instead reported that 18.8% of 1119 patients experienced stent graft migration within a follow-up period of three years. The percental decrease of patients suffering from stent graft migration is promising, but the amount of patients experiencing migration is still considered problematic.

The main purpose of this work is to investigate the possibilities of using Fluid-Structure Interaction (FSI) simulations on stent grafts to assess the forces causing migration of the non-fixated distal attachments when subjected to a pulsating flow. A study performed by Malina et al. [5] demonstrates that these forces range between 2 and 3.4 N.

Two different numerical approaches are applied in the FSI simulations; one based on the Finite Element (FE) method and another based on the Finite Volume (FV) method. A second purpose is thus the comparison between these two approaches, which is considered to be highly interesting from an academical point of view and is expected to give further input for evaluation of the results.

1.3 Method

The computational work is divided into two parallel studies using two different softwares. The softwares, OpenFOAM-1.6-ext and LS-DYNA 971 R5.1.1, use different numerical approaches for simulating the flow, the structural behavior and the coupling between the two phases. The OpenFOAM (OF) solver is based on FV discretization and the method used in LS-DYNA (LD) is an FE based Arbitrary Lagrangian-Eulerian (ALE) formulation. To gain confidence in the results the same simulations are set up in both codes and the results are compared.

The first case is a straight, *rigid* cylindrical pipe subjected to a steady, laminar flow of water. This is done in order to compare the flow characteristics when solving with OF (FV formulation) and LD (FE formulation), respectively. Furthermore, both numerical solutions are validated against the analytical solution for a laminar fully developed pipe flow (see Appendix A).

The second case is a coupled FSI analysis, simulating a flow of water within a lightweight, *flexible*, thin-walled pipe with a diameter of $d = 0.014$ m and a predefined angle of 90 degrees between the inlet and outlet normal vectors, see Figure 1.3. Also, in attachment with the bent pipe there are rigid inlet and outlet sections. The flexible pipe is given material properties extracted from the work done by Li and Kleinstreuer [1, 6], which corresponds to a real stent graft.

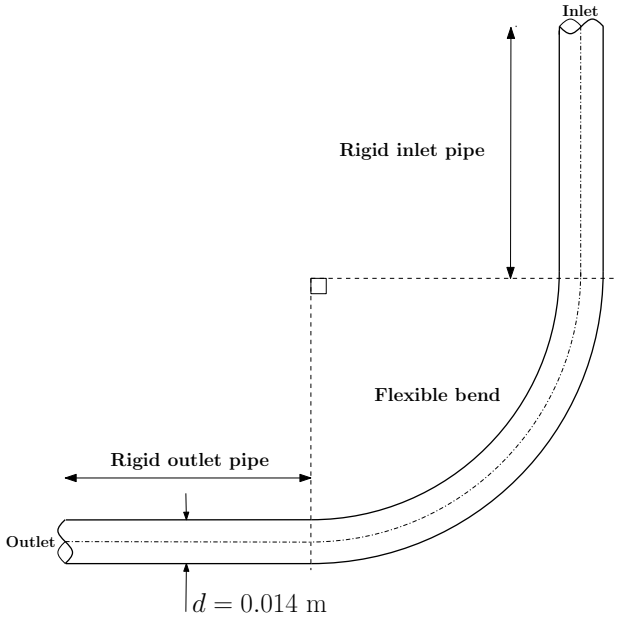

Figure 1.3: The geometry of the setup.

Two different flow scenarios are studied; a steady inlet velocity and a sinusoidal inlet velocity. The analyses are performed using the FSI modules included in both OF and LD. As indicated in Section 1.2, the main goal is to determine the forces arising in the attachments of the flexible, bent pipe due to the mechanical interaction between the fluid flow and the structure. For the steady case an additional simple momentum balance calculation (see Appendix B) is performed to obtain estimates of the forces. This is done in order to gain further confidence in the results. Also, since using two different softwares with two different numerical approaches, a comparison is made to highlight differences and similarities between the different solution procedures.

Since the FV discretization in OF requires volume elements in both the fluid and structural domain, the simulations in OF necessitates the use of a certain material thickness for the part of the pipe corresponding to a stent graft. In LD, however, the FE formulation allows the use of shell elements to simulate the thin-walled structure. The virtual material thickness is here set in correspondence to the element thickness used in OF.

The forces induced by the Fluid-Structure Interaction are extracted as normal forces at the inflow and at the outflow of the flexible bend section. In OF this is done by multiplying the normal stress with respective area for each cell and summarizing them. In LD they are extracted as nodal forces at each shell element and then summarized.

1.4 Limitations

- The software modules used in this study do not provide the possibility of using a turbulence model for the calculation of the fluid flow. Since the grids used are too coarse to fully resolve the smallest scales of any possible occurrence of turbulence, uncertainties arise concerning the accuracy of the flow field simulations. Consequently, this may affect the calculation of the forces acting on the graft attachments and has to be considered as an additional source of error.

- A reasonable gauge pressure corresponds to a blood pressure of 80 mmHg. That is, the internal pressure causes the bent portion of the pipe to experience stresses (and possible expansion) already in a static state. However, due to convergence problems,

this pressure condition is not taken into account in the simulations. Hence, the forces extracted from the computational analyses are induced *only* by the fluid motion.

1.5 Assumptions and simplifications

- In order to achieve managable calculation times, a symmetry condition is introduced for the setups in both softwares. The use of symmetry is argued to be applicable since the solution for a *laminar* pipe flow should be symmetric. Moreover, in case of occurence of turbulence the symmetry condition is considered *not* to give rise to more sources of errors than the already insufficiently resolved turbulence.
- The calculations are performed using water as the fluid medium.
- A bulk modulus for water of the magnitude 10^6 is assumed to be adequate to avoid compressibility effects in LD.
- Only *one* of the distal extensions is simulated.
- The geometry is generalized in such a way that the curvature of the bent pipe is assumed to be circular and, as mentioned in Section 1.3, the angle between the inlet and outlet normal vectors is set to 90 degrees.
- The sinusoidal flow is assumed to pulsate with a frequency corresponding to a heart rate of 60 bpm.
- The structure is considered to be in an initial stressfree state. That is, stresses that arise due to the initial bending of the pipe are neglected in the analysis.
- The flexible pipe material is assumed to have a constant density, i.e. not dependent upon the stretching or compression of the material.
- Modelling a woven stent graft material with a reinforcing structure is considered too complex and time consuming. Hence, the pipe walls are modelled as smooth. Moreover, the material is considered both isotropic and homogeneous, disregarding any anisotropy present due to a stented structure. For this reason, the flexible pipe is from now on referred to as an Endovascular Graft (EVG).

1.6 Sustainability and environmental aspects

If the knowledge from this project (as well as subsequent ones) leads to improvements lowering the percentage of patients experiencing stent graft migration and reducing the number of fatalities, this is of great weight from a sustainability point of view. With further confidence in the stent graft's performance, there can be a reduced amount of follow up sessions and emergency surgeries, lowering the overall material cost and in the long run lessening the impact on the environment.

2 Theory

This section presents a general overview of some fundamental concepts of continuum mechanics along with basic notations, followed by more detailed explanations of the theory behind the FE based ALE approach used in LD as well as the FV formulation used in the OF solver.

2.1 Notations

Consider three domains (see Figure 2.1), the spatial domain (B), the material domain (B_0) and the arbitrary referential domain ($\tilde{B}$). Let t denote the open time interval $t \in]0, T[$ and let $\mathbf{X}$, $\tilde{\mathbf{X}}$ and $\mathbf{x}$ denote the material, referential and spatial coordinates. A time derivative of some function ζ is required in order to describe the continuum, where ζ can be defined as a function of previous mentioned coordinates. Hence [7]:
The spatial time derivative

$$\frac{\mathrm{d}\zeta}{\mathrm{d}t} = \frac{\partial \zeta(\mathbf{x}, t)}{\partial t} \mid_x \tag{2.1}$$

The material time derivative

$$\dot{\zeta} = \frac{\mathrm{d}\zeta(\mathbf{X}, t)}{\mathrm{d}t} \mid_X \tag{2.2}$$

The referential time derivative

$$\tilde{\zeta} = \frac{\mathrm{d}\zeta(\tilde{\mathbf{X}}, t)}{\mathrm{d}t} \mid_{\tilde{X}} \tag{2.3}$$

The spatial domain, and the image of B_o at time t, is defined through the material map $\boldsymbol{\varphi}$. Assume B to be the image of $\tilde{B}$ at time t under the mesh map $\tilde{\boldsymbol{\varphi}}$. The material motion is characterized through the material map $\boldsymbol{\varphi}$ from the material configuration B_0 to spatial configuration B with:

$$\mathbf{x} = \boldsymbol{\varphi}(\mathbf{X}, t) : B_0 \to B,$$

its linear tangent map:

$$\mathbf{F} = \nabla_{\mathbf{X}} \boldsymbol{\varphi}(\mathbf{X}, t) : TB_0 \to TB,$$

and its Jacobian:

$$J = \det \mathbf{F}.$$

The Jacobian define the following relations between spatial and material vectorial area elements and infinitesimal volume elements respectively:

$$d\mathbf{a} = J\mathbf{F}^{-\mathrm{T}} \cdot d\mathbf{A}, \qquad dv = JdV.$$

Similarly, the vector map $\tilde{\boldsymbol{\varphi}}$ from the referential $\tilde{B}$ to the spatial B configuration, with the mesh motion characterized by:

$$\mathbf{x} = \tilde{\boldsymbol{\varphi}}(\tilde{\mathbf{X}}, t) : \tilde{B} \to B$$

and its related linear tangent map and Jacobian:

$$\tilde{\mathbf{F}} = \nabla_{\tilde{\mathbf{X}}} \tilde{\boldsymbol{\varphi}}(\tilde{\mathbf{X}}) : T\tilde{B} \to TB, \qquad \tilde{J} = \det \tilde{\mathbf{F}}.$$

The Jacobian is used to define the following relations between spatial and referential vectorial area and volume elements as:

$$d\mathbf{a} = \tilde{J}\tilde{\mathbf{F}}^{-\mathrm{T}} \cdot d\tilde{\mathbf{A}}, \qquad dv = \tilde{J}d\tilde{V}.$$

Transformation between the different formulations are based on pull-back and push-forward operations in terms of the material deformation gradient $\mathbf{F}$, the mesh deformation gradient $\tilde{\mathbf{F}}$ and their Jacobians J and $\tilde{J}$, see Figure 2.1.

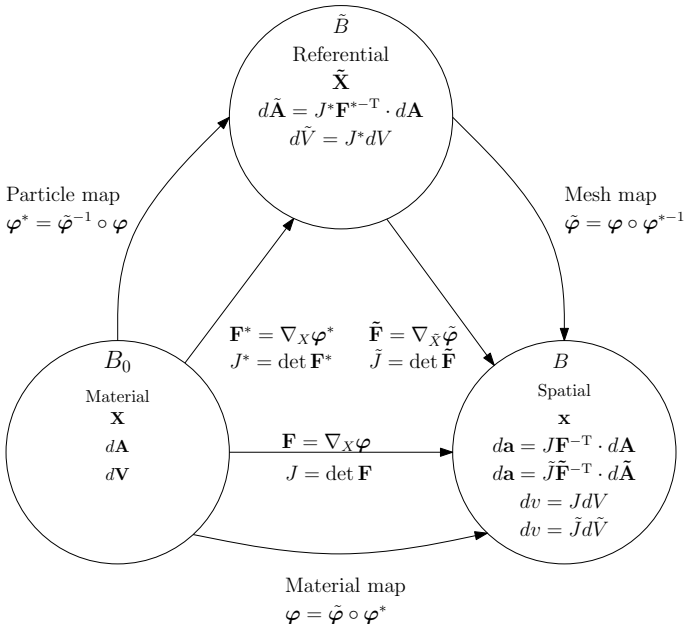

Figure 2.1: Material, referential and spatial domains with corresponding mappings.

With the mappings $\mathbf{x} = \varphi(\mathbf{X}, t)$ and $\mathbf{x} = \tilde{\boldsymbol{\varphi}}(\tilde{\mathbf{X}}, t)$ one thus find that the material time derivatives of the quantity $\zeta = \zeta(\mathbf{x}, t)$ (see equation (2.2)-(2.3)), can be related via:

$$\dot{\zeta} = \frac{\partial \zeta}{\partial t} + \nabla \cdot \mathbf{v}, \quad \tilde{\dot{\zeta}} = \frac{\partial \zeta}{\partial t} + \nabla \cdot \mathbf{v}_G$$

where $\mathbf{v}_G$ is sometimes named the "grid velocity". Upon eliminating the spatial time derivative in equation (2.1) one obtains the relationships between material velocities in the different domains

$$\dot{\zeta} = \tilde{\dot{\zeta}} + \nabla \cdot (\mathbf{v} - \mathbf{v}_G) = \tilde{\dot{\zeta}} + \nabla \cdot \mathbf{c}, \tag{2.4}$$

with

$$\mathbf{c} = \mathbf{v} - \mathbf{v}_G \tag{2.5}$$

where $\mathbf{c}$ is commonly called the "convective velocity". For example it is now possible to immediately express the acceleration, appearing in the momentum balance relation, as:

$$\mathbf{a} = \dot{\mathbf{v}} = \mathbf{v}_G + \nabla \cdot \mathbf{c}$$

2.1.1 ALE, Lagrangian and Eulerian descriptions

Three descriptions can be defined by relating the reference coordinate with the material or spatial coordinate. Firstly, for Lagrangian description (see Figure 2.3a), $\tilde{\mathbf{X}} = \mathbf{X}$, hence the convective velocity $\mathbf{c} = 0$ and the mesh motion is equal to the velocity of the material. With $\mathbf{X} = \mathbf{x}$, the mapping function $\tilde{\boldsymbol{\varphi}}$ becomes an identity map and the grid velocity, $\mathbf{v}_G = 0$. The mesh is then fixed and corresponds to the Eulerian description (the fixed background grid see Figure 2.3a). When $\tilde{\mathbf{X}} \neq \mathbf{x}$ and $\tilde{\mathbf{X}} \neq \mathbf{X}$, the mesh moves with an arbitrary velocity in space. This is the ALE description [7, 8].

2.2 Physical conservation principles

Consider an isothermal continuum element in an arbitrary volume V bounded by a surface S at a time t. The continuum is then governed by the fundamental conservation laws for mass and linear momentum [9], i.e:

$$\frac{\mathrm{d}}{\mathrm{d}t}\int_V \rho \,\mathrm{d}V = 0, \tag{2.6}$$

$$\frac{\mathrm{d}}{\mathrm{d}t}\int_V \rho\mathbf{v} \,\mathrm{d}V = \int_V \rho\mathbf{b} \,\mathrm{d}V + \int_S \mathbf{t}^{(\mathbf{n}_f)} \,\mathrm{d}S \tag{2.7}$$

where ρ is the continuum density (whether it is a fluid or solid constituent), $\mathbf{v}$ is the constituent velocity which, pertinent to a Cartesian coordinate system with basis vectors in the Eulerian frame $[\mathbf{e}_i]_{i=x,y,z}$, take on the components $[\mathbf{v}_i]_{i=x,y,z}$. Moreover, $\mathbf{b}$ is the body force vector with components $[\mathbf{b}_i]_{i=x,y,z}$ and $\mathbf{t}^{(\mathbf{n}_f)}$ is the vectorial force per unit surface area acting on the boundary S.

By using Reynold's transport theorem, i.e.

$$\frac{\mathrm{d}}{\mathrm{d}t}\int_V \phi \,\mathrm{d}V = \int_V \left(\frac{\partial\phi}{\partial t} + \nabla\cdot(\phi\mathbf{v})\right)\mathrm{d}V \tag{2.8}$$

with $\phi = \phi(\mathbf{x}, t)$ being an arbitrary spatial quantity, the law of mass conservation (2.6) can be written as

$$\int_V \left(\frac{\partial\rho}{\partial t} + \nabla\cdot(\rho\mathbf{v})\right)\mathrm{d}V = 0 \tag{2.9}$$

where ∇ is the spatial vector gradient operator with components $[\nabla_i]_{i=x,y,z} = \left[\frac{\partial}{\partial x}, \frac{\partial}{\partial y}, \frac{\partial}{\partial z}\right]$. The *Cauchy stress theorem* states that there exists a second order tensor $\boldsymbol{\sigma}$ related to the traction such that

$$\mathbf{t}^{(\mathbf{n}_f)} = \boldsymbol{\sigma}\cdot\mathbf{n}_f \tag{2.10}$$

where $\mathbf{n}_f$ is the outwards pointing unit normal vector of the outer surface. The tensor $\boldsymbol{\sigma}$ is called the *Cauchy stress tensor*. By using relation (2.10) together with the divergence theorem, the right hand side of the momentum conservation law (equation (2.7)) can be rewritten. By also introducing Reynold's transport theorem and cancelling out the zero value terms due to mass conservation (equation (2.9)), the momentum equation can be expressed as

$$\frac{\mathrm{d}}{\mathrm{d}t}\int_V \rho\mathbf{v} \,\mathrm{d}V = \int_V (\boldsymbol{\sigma}\cdot\nabla + \rho\mathbf{b}) \,\mathrm{d}V. \tag{2.11}$$

2.2.1 Viscous fluids

For an infinitesimal fixed isothermal Control volume (CV) dV, (see Figure 2.2) *localization* of equation (2.9) yields that

$$\boxed{\frac{\partial\rho}{\partial t} + \nabla\cdot(\rho\mathbf{v}) = 0} \tag{2.12}$$

Equation (2.12) is the continuum version of the mass conservation equation and is often referred to as the *equation of continuity*.

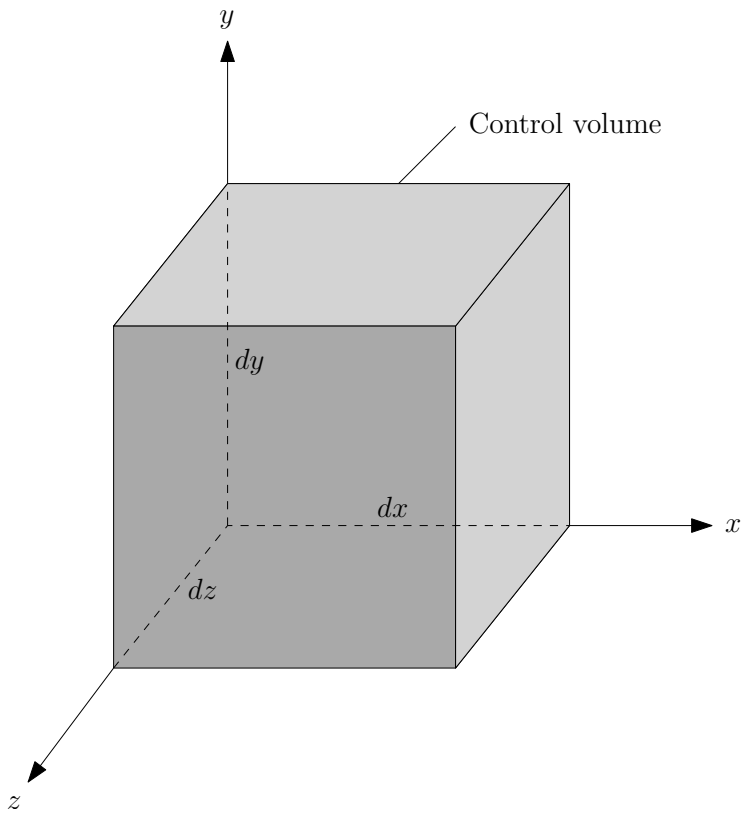

Figure 2.2: An infinitesimal control volume dV.

By using a similar reasoning for the conservation of momentum, the differential *momentum equation* for an infinitesimal CV (in vector form) read

$$\frac{\mathrm{d}}{\mathrm{d}t}(\rho\mathbf{v}) = \boldsymbol{\sigma}\cdot\nabla + \rho\mathbf{b} \tag{2.13}$$

where $\frac{\mathrm{d}\mathbf{v}}{\mathrm{d}t} = \frac{\partial\mathbf{v}}{\partial t} + \mathbf{v}\cdot\nabla\mathbf{v}$ is the material derivative.

The general assumption for fluids is that the stress is a function of pressure and the velocity gradient [9], i.e.

$$\boldsymbol{\sigma} = \boldsymbol{\sigma}(p, \nabla\mathbf{v})$$

and the constitutive relation for a viscous fluid is usually assumed to be additatively decomposed according to

$$\boldsymbol{\sigma} = -p\mathbf{I} + \boldsymbol{\tau}. \tag{2.14}$$

Introducing (2.14) into (2.13) yields the differential momentum equations for a viscous fluid as

$$\frac{\mathrm{d}}{\mathrm{d}t}(\rho\mathbf{v}) = -\nabla p + \nabla\cdot\boldsymbol{\tau} + \rho\mathbf{b} \tag{2.15}$$

where ∇p is the pressure gradient across the CV and $\boldsymbol{\tau}$ is the viscous stress tensor defined as

$$\boldsymbol{\tau} = \begin{bmatrix} \tau_{xx} & \tau_{xy} & \tau_{xz} \\ \tau_{yx} & \tau_{yy} & \tau_{yz} \\ \tau_{zx} & \tau_{zy} & \tau_{zz} \end{bmatrix}. \tag{2.16}$$

The viscous stresses can be written as [10]

$$\tau_{xx} = 2\mu\frac{\partial v_x}{\partial x}, \qquad \tau_{yy} = 2\mu\frac{\partial v_y}{\partial y}, \qquad \tau_{zz} = 2\mu\frac{\partial v_z}{\partial z},$$
$$\tau_{xy} = \tau_{yx} = \mu\left(\frac{\partial v_x}{\partial y} + \frac{\partial v_y}{\partial x}\right), \quad \tau_{xz} = \tau_{zx} = \mu\left(\frac{\partial v_z}{\partial x} + \frac{\partial v_x}{\partial z}\right), \quad \tau_{yz} = \tau_{zy} = \mu\left(\frac{\partial v_y}{\partial z} + \frac{\partial v_z}{\partial y}\right) \tag{2.17}$$

where μ is the coefficient of dynamic viscosity. Substituting (2.17) into (2.15) gives the differential momentum equation for a Newtonian fluid[2] as

$$\boxed{\frac{\mathrm{d}}{\mathrm{d}t}(\rho\mathbf{v}) = -\nabla p + \mu\nabla^2\mathbf{v} + \rho\mathbf{b}.} \tag{2.18}$$

Equation (2.18) is more commonly known as the *Navier-Stokes equation*.

2.2.2 Elastic solids

For an elastic solid the Cauchy stress is a function of the displacement gradient [9], i.e.

$$\boldsymbol{\sigma} = \boldsymbol{\sigma}(\nabla\mathbf{u})$$

where $\mathbf{u} = \mathbf{r} - \mathbf{r}_0$ denotes the displacement vector relating the current material point position, $\mathbf{r}$, to the initial material point position, $\mathbf{r}_0$. Since the solid is assumed to be elastically compressible, the pressure is also a function of $\nabla\mathbf{u}$ and is hence not needed as an argument for the stress.

When considering finite deformations, alternatives to the Cauchy stress tensor are often used. The *Piola-Kirchhoff stress tensors* are examples of such alternatives. They express the stress relative to a reference configuration, whereas the Cauchy stress tensor expresses the stress in relation to the present configuration.

The *first* Piola-Kirchhoff stress tensor, $\boldsymbol{\mathcal{P}}$, relates forces in the *present* configuration with areas in the *reference* ("material") configuration. The first Piola-Kirchhoff stress tensor is related to the Cauchy stress tensor as

$$\boldsymbol{\mathcal{P}} = J\boldsymbol{\sigma}\cdot\mathbf{F}^{-\mathrm{T}} \tag{2.19}$$

where $\mathbf{F}$ is the deformation gradient tensor defined as

$$\mathbf{F} = \mathbf{I} + (\nabla_{\mathbf{X}}\mathbf{u})^{\mathrm{T}} \tag{2.20}$$

where $\nabla_{\mathbf{X}} = \nabla\cdot\mathbf{F}^{-\mathrm{T}}$ is the material gradient operator.

The *second* Piola-Kirchhoff stress tensor, $\boldsymbol{\Sigma}$, is further defined in terms of the first Piola-Kirchhoff stress tensor as

$$\boldsymbol{\Sigma} = \mathbf{F}^{-1}\cdot\boldsymbol{\mathcal{P}} \tag{2.21}$$

and the relation between the second Piola-Kirchhoff stress tensor and the Green-Lagrangian strain tensor is governed by the constitutive equation for a St. Venant-Kirchhoff material, i.e.

$$\boldsymbol{\Sigma} = 2G\mathbf{E} + \lambda\,\mathrm{tr}\,(\mathbf{E})\mathbf{I} \tag{2.22}$$

where G and λ are the *Lamé's coefficients* and $\mathbf{E}$ is the Green-Lagrangian strain tensor defined as

$$\mathbf{E} = \frac{1}{2}(\mathbf{F}^{\mathrm{T}}\cdot\mathbf{F} - \mathbf{I}). \tag{2.23}$$

Once again, using localization, equation (2.11) can now be expressed in terms of the first or the second Piola-Kirchhoff stress tensor as

$$\boxed{\rho_0\frac{\mathrm{d}\mathbf{v}}{\mathrm{d}t} = \boldsymbol{\mathcal{P}}\cdot\nabla_{\mathbf{X}} + \rho_0\mathbf{b}} \tag{2.24}$$

and

$$\boxed{\rho_0\frac{\mathrm{d}\mathbf{v}}{\mathrm{d}t} = (\mathbf{F}\cdot\boldsymbol{\Sigma})\cdot\nabla_{\mathbf{X}} + \rho_0\mathbf{b}.} \tag{2.25}$$

[2] i.e. a fluid that follows the linear law of resistance, $\tau = \mu\frac{dv_x}{dy}$, postulated by Sir Isaac Newton in 1687.

2.3 Numerical approaches in LS-DYNA and OpenFOAM

As stated in Section 1.3 the two softwares are based on two different numerical approaches for solving the interaction between the solid and fluid phases. The case in LD was set up using an FE based Multi Material ALE (MMALE) formulation where a Lagrangian structure is constrained within a fixed, independent Eulerian mesh (see Figure 2.3a). In contrast, the solver used in OF is fully based on an FV formulation where the solid and fluid meshes are allowed to share nodes (see Figure 2.3b).

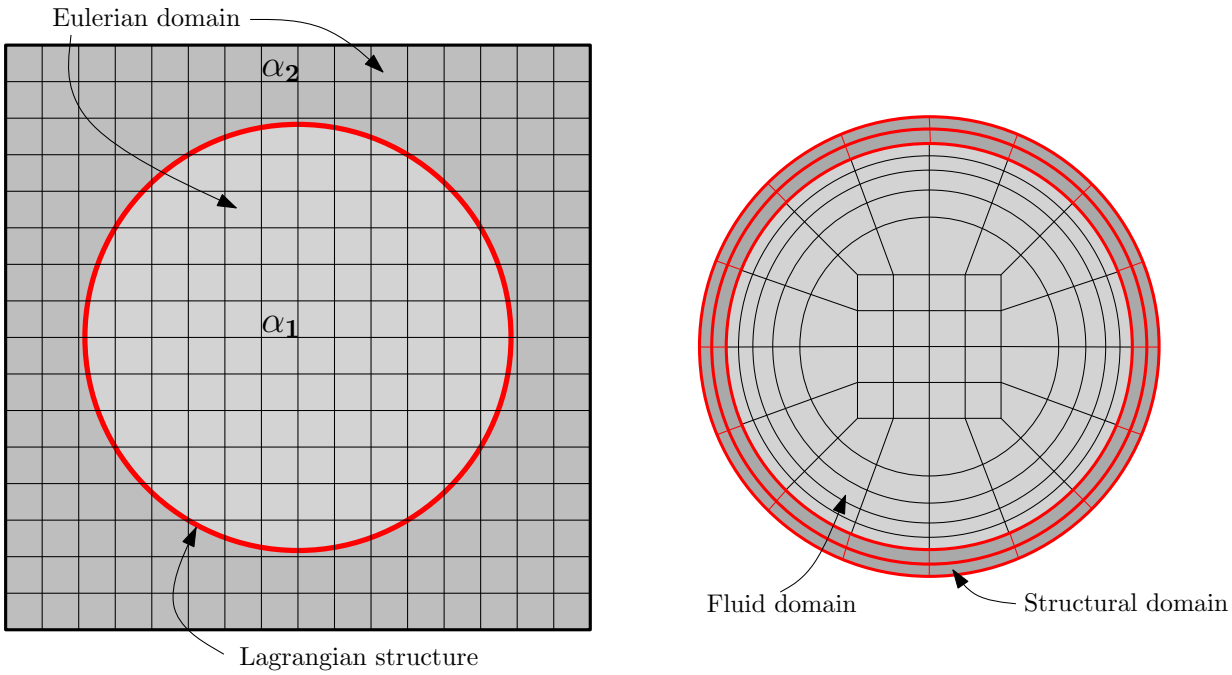

(a) ALE, constrained Lagrangian in solid method

(b) FV

Figure 2.3: Schematic figures of MMALE and FV formulation. In a) the shaded areas denote the Eulerian domain and the circle denotes the Lagrangian structure. In b) the darker shaded area indicates structural elements while the brighter area denotes fluid elements.

The FE and FV methods are numerical techniques for solving partial differential equations. Both approaches use a meshed geometry to calculate values in a finite number of discrete locations (called elements or cells), but the calculation procedure differs between the two methods. The main idea in the FE method is to establish, so called, shape functions $v(x)$ that element-wise approximate the continuous function $u(x)$ which is the solution to the partial differential equation formulated in weak form. The approximation $v(x)$ is usually a polynomial describing how $u(x)$ varies across the element, and the approximation can be regarded as some kind of interpolation. It is assumed that the values are known at certain points of the element and these points are called *nodes*. In the FE method these are usually located at the element vertices [11], see Figure 2.4a.

In the FV method, the computational nodes are instead enclosed by a finite number of infinitesimal control volumes. Figure 2.4b shows an example of a two-dimensional FV mesh, where nodes are denoted by a $\bullet$-symbol and upper case letters while CV face centers are denoted by a $\times$-symbol and lower case letters. Using the divergence theorem, the volume integrals of the partial differential equations containing a divergence term may be converted into surface integrals. This way the fluxes of the quantities can be evaluated at each control volume face. Considering the laws of conservation (see Section 2.2.1), the flux *leaving* a certain CV has to be identical to the flux *entering* an adjacent one. By

discretizing the surface integrals [12], and assuming that the rate of change is polynomial across the cell, the fluxes can then be used to evaluate the sought after variables in each node.

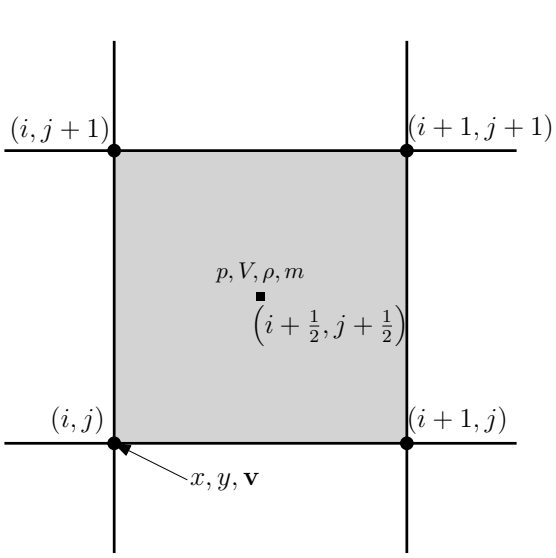

(a) Four-noded FE element: variable positions corresponding to the ALE formulation.

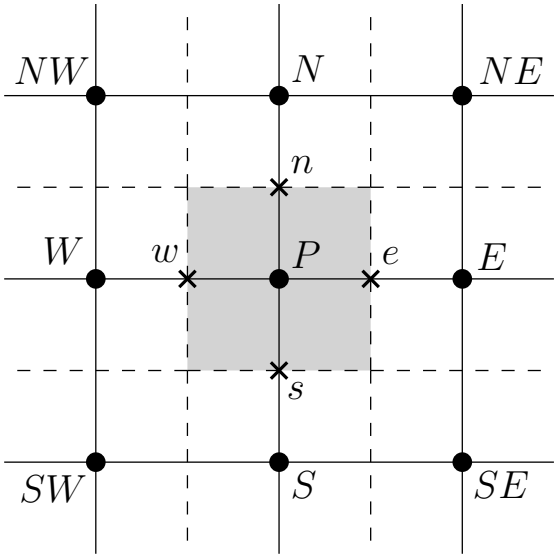

(b) Structured 2D FV mesh: velocities and pressure computed in nodes (•), fluxes computed at control volume surfaces (×).

Figure 2.4: Schematic figures of FE and FV formulation.

Since the applied ALE formulation is based on an FE approach the element nodes are positioned at the element vertices (see Figure 2.4a). These nodes contain the mesh coordinates, x and y, and the velocity, $\mathbf{v}$. The mass, m, and volume, V, are instead defined in the center of the element, $\left(i+\frac{1}{2}, j+\frac{1}{2}\right)$, where also the pressure, p, and the material density, ρ, are calculated.

Each of the element solution variables have to be transported. Since the velocities are stored in the element vertices and the density is stored in the element center, this gives rise to difficulties of advecting the momentum (which is a product of density and velocity). In this ALE approach these difficulties are overcome by advecting the nodal momentum instead of the velocity, in order to ensure conservation of momentum [13]. The procedure is to modify an element-centered advection algorithm to advect the node-centered momentum. This is done by constructing auxiliary sets of element-centered variables from the (nodal) momentum, advect them and then reconstruct the new (nodal) velocities from the auxiliary variables.

The chosen ALE method (MMALE, see Section 2.4) demands two or more materials to be defined within the Eulerian mesh; the first one, α_1, in the elements constrained by the Lagrangian structure and a second one, α_2, in the surronding elements. This is not the case in OF where the calculations are performed for a single fluid material.

Since the Eulerian and Lagrangian meshes are *not* coupled nodewise in LD, a coupling algorithm is needed to define the contact interfaces between the Lagrangian mesh and the materials defined in the Eulerian mesh. There are several coupling methods applicable for the ALE formulation. In LD both penalty based and constraint based coupling methods are available. Thus, a brief description of the two approaches is provided in Section 2.4.

In OF the coupling between the phases is governed by a traction vector, consisting of the fluid pressure and the shear stresses arising from the fluid-structure interaction. The traction vector is obtained by calculating the flow field and is then introduced into

the equations for the structure. Subsequently, the structural displacements are solved for and both the fluid and solid meshes are deformed accordingly. The displacement of the fluid-structure interface then appears as a boundary condition for the fluid phase in the following time step and the solution procedure is repeated.

2.4 The Arbitrary Lagrangian-Eulerian formulation in LS-DYNA

In fluid-structure interaction problems where the fluid mesh, if treated as Lagrangian, would undergo massive deformation near the structure, causing the timestep to take an unacceptable small value, ALE is of great use [13]. The method is sometimes used to create a new undistorted mesh for the deforming domain which makes it possible to continue the calculations. In the case of the EVG, the structure is treated as a Lagrangian and the fluid as a fixed Eulerian mesh. This way any distortions of the fluid mesh due to displacement of the EVG structure is completely avoided. The details of LD's ALE implementation are not fully available. Nevertheless, a conceptual overview is provided in this section.

2.4.1 Governing equations

The chosen method in LD solves the isothermal fluid problem using *Eulerian descriptions* of the continuity equation and the Navier-Stokes equations (see equation (2.12) and (2.18)) discussed in section 2.2.1. That is, the grid velocity is zero and hence, according to equation (2.5), the convective velocity equals the material velocity, i.e. $\mathbf{c} = \mathbf{v}$. Neglecting all the body forces, the governing equations for the compressible fluid problem then become

Continuity equation

$$\frac{\partial \rho}{\partial t} + \nabla \cdot (\rho \mathbf{v}) = 0 \tag{2.26}$$

Momentum equation

$$\frac{\mathrm{d}}{\mathrm{d}t}(\rho \mathbf{v}) = -\nabla p + \mu \nabla^2 \mathbf{v} \qquad \text{in} \quad \mathbf{B} \tag{2.27}$$

The governing equation for the structural behavior, expressed in the Lagrangian framework, is the conservation of momentum:

$$\rho_0 \frac{\mathrm{d}\mathbf{v}}{\mathrm{d}t} = \boldsymbol{\mathcal{P}} \cdot \nabla_{\mathbf{X}} + \rho_0 \mathbf{b} \qquad \text{in} \quad \mathbf{B}_0 \tag{2.28}$$

where $\boldsymbol{\mathcal{P}}$ is the first Piola-Kirchhoff stress tensor (see equation (2.19) in Section 2.2.2).

2.4.2 Multi Material ALE

In Eulerian and ALE-formulation it is possible to allow two or more materials in one element in a fixed mesh. In LD this is refereed to as the Multi Material ALE (MMALE) method where the elements contain a certain volume fraction of each material. The volume fraction represented by α_i^e in element e of material i is expressed as:

$$\alpha_i^e = \frac{V_i^e}{V^e} \tag{2.29}$$

where V_i^e represents the material volume and V_i the element volume. Furthermore the sum of the volume fractions must always equal 1 within one element such that:

$$\sum_{i=1}^{n} \alpha_i^e = 1 \tag{2.30}$$

As the mass fluxes between elements, the initially well defined material boundary is replaced by a transition region where α_i^e drops from 1 to 0. If the interface was to be tracked by either the donor cell or van Leer advection scheme, it would be severely smeared [14]. Instead interface reconstruction is used, where the mixed elements are cut with a plane separating the materials (see Figure 2.5). The orientation of the plane is controlled by the gradient of the volume fraction field, which is governed by the Lagrangian structure. When the structure moves, the volume fractions are updated and the interface plane is reconstructed accordingly. The movement of the structure is determined by the fluid structure interaction, for which a coupling algorithm is needed.

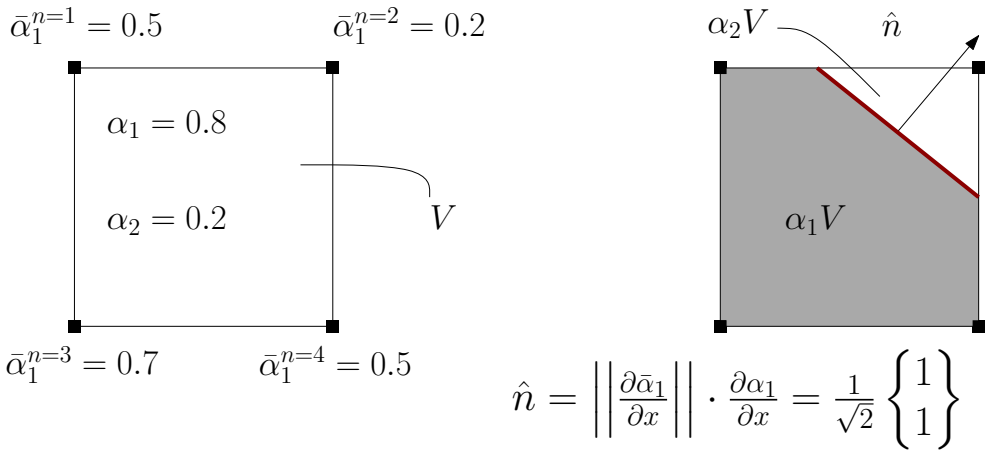

Figure 2.5: MMALE with two materials.

2.4.3 Fluid-structure interaction

The most fundamental question when dealing with fluid-structure interaction is arguably whether the fluid and structural parts are in contact with eachother. This section presents the basics of the contact based methods, regarding the fluids and solids as compounds of particles. LD does not treat the phases as compounds of particles; instead the coupling is handled by nodal contacts. However, the concept of the coupling is similar, considering the nodes as particles. Hence, the following reasoning is considered valid for explaining the main idea behind the coupling methods.

The conditions for finding possible collisional contacts between particles can be written as [15]

$$||\mathbf{X}_f - \mathbf{X}_s|| \ \leq \ r_f + r_s \tag{2.31}$$

and

$$\mathbf{n} \cdot (\mathbf{v}_f - \mathbf{v}_s) \ \leq \ 0 \tag{2.32}$$

where $\mathbf{X}_f$ and $\mathbf{X}_s$ denote the positions of the fluid and solid particles, respectively, r_f and r_s denote their radii, $\mathbf{n}$ is the unit surface normal at the contact point and $\mathbf{v}_f$ and $\mathbf{v}_s$ represent the fluid and solid velocities, respectively.

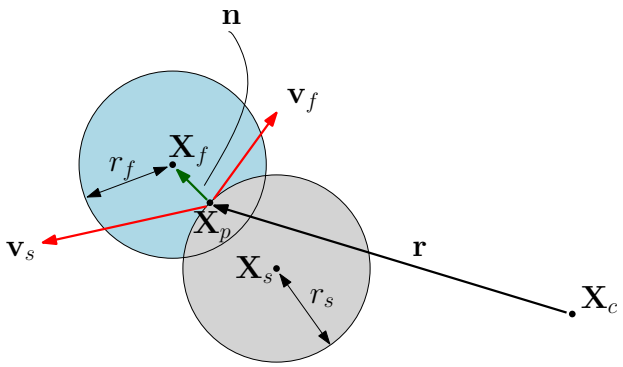

Figure 2.6: Collision between fluid and solid particles.

Figure 2.6 shows a collision between a fluid and solid particle. The solid particle velocity is expressed as $\mathbf{v}_s = \mathbf{v}_{par} + \omega \times \mathbf{r}$, where $\mathbf{v}_{par}$ and ω are the linear and angular velocities of the corresponding solid particle, respectively.

From Figure 2.6 and equation (2.31) it can be concluded that the fluid and solid particles overlap eachother at the contact point $\mathbf{X}_p = \mathbf{X}_s + r_s\mathbf{n}$. Equation (2.32) then implies that the relative velocity of the fluid particle with respect to the solid particle along the normal direction is less than zero. A positive value of the relative velocity would instead mean that the particles are no longer interpenetrated. This would be the case in a future time step when the particles would be separated and hence not in contact with eachother anymore.

To resolve all contacts between the fluid and solid phases a coupling algorithm is needed. LD offers a penalty based coupling method as well as a constraint based one. The penalty based method computes contact forces, $\mathbf{F}_{contact}$, between the fluids and solids to prevent the interpenetration of the phase surfaces. The contact force is defined as

$$\mathbf{F}_{contact} = k_s d\mathbf{n} + k_d(\mathbf{v}_{rel} \cdot \mathbf{n})\mathbf{n} \tag{2.33}$$

where k_s and k_d represent the stiffness and damping coefficients respectively, d denotes the penetration depth or the overlap between the colliding surfaces, $\mathbf{n}$ is the unit surface normal at the contact point and $\mathbf{v}_{rel}$ is the relative velocity between the fluid and solid nodes.

Finding a suitable value for the stiffness parameter can be somewhat troublesome and is a matter of trial and error. Another shortcoming with the penalty based method is that it requires very small time steps to stably resolve collisions.

The constraint based coupling method provides another way to resolve the fluid-solid contacts. This method connects the velocities of the fluid and solid bodies through an impulse description, rather than affecting their accelerations through a contact force. Unlike the penalty based method, the constraint based method does not conserve the kinetic energy [14]. Figure 2.7 shows a conceptual explanation of the constraint based coupling method used in LD where a collision between the phases is considered perfectly inelastic.

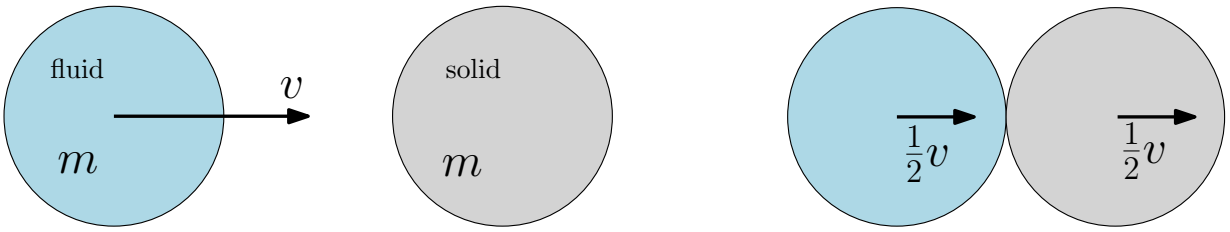

(a) Before impact (b) After impact

Figure 2.7: Schematic figures of a fluid particle a) before and b) after colliding with a solid particle for the constraint based coupling method used in LD.

Before impact of the fluid and solid particles (see Figure 2.7a) the momentum, $\hat{p}$, and kinetic energy, W_k, are

$$\hat{p}_0 = mv \tag{2.34}$$

$$W_{k_0} = \frac{1}{2}mv^2 \tag{2.35}$$

where subscripts 0 refers to values at time $t = 0$, i.e. before impact.

After a perfectly inelastic collision (see Figure 2.7b), the particles stick together with a conserved momentum

$$\hat{p}_1 = \frac{1}{2}mv + \frac{1}{2}mv = mv = \hat{p}_0, \tag{2.36}$$

but with a loss in kinetic energy

$$W_{k_1} = \frac{1}{4}mv^2 < W_{k_0}. \tag{2.37}$$

2.4.4 Solution procedure of the LS-DYNA solver

A non-symmetric convective term, stemming from the convective velocity c, poses major difficulties associated with time integration. If considering a Lagrangian description the relative motion is zero due to the material and referential systems being identical and thus the convective term would disappear. In order to solve the ALE equations LD applies the Operator Split method. The approach is used in order to achieve less complex problems, divided into two or more sets which are solved sequentially.

The structural equations (2.28) are solved with the fluid pressure and shear stresses from equation (2.27) on the interface as a Neumann boundary condition. The solution gives the structural velocities which are equal to the grid velocity, $\mathbf{v}_G$. The structure's new position updates the interface with the volume fractions for the fluid materials.

1. Perform a Lagrangian time step
2. Perform an advection step.

   i) Move the material interface.

   ii) Calculate the transport of element-centred variables

   iii) Calculate the momentum transport and update the velocity.

In the first substep, the mesh moves with the material and the changes in velocity and internal energy due to internal and external forces are calculated. When the new configuration for the Lagrangian substep is reached the advection (or Eulerian) substep takes place. Now a new nodal pattern has to be defined, unless it has been predefined by the user, as is the case for this study, where Eulerian formulation is used and the mesh displacements set to zero. When the nodal pattern has been defined, the solutions variables need to be remapped to the arbitrary position with an advection algorithm, computing the transport of mass, internal energy and momentum across cell boundaries.

2.4.5 Advection method

When the nodal repositioning has been performed, the solution from the previous, distorted configuration need to be mapped onto the new one [14]. This is known as the advection step. Two assumptions are made for the remap step, first of all, the topology of the mesh is fixed and secondly, during a step, the mesh motion is less than the characteristic lengths

of the neighbouring elements, i.e the Courant-Friedrichs-Lewy (CFL) number, should be less than one [13]. The algorithms used to perform the remap step are called advection algorithms referring to the scalar conservation equation (2.38):

$$\frac{\partial \phi}{\partial t} + a(x)\frac{\partial \phi}{\partial t} = 0 \tag{2.38}$$

A beneficial advection algorithm is stable, conservative, accurate and monotonic. Although several of the solution variables are not governed by conservation equations, it is vital that they remain unchanged during the remap step. Conservation of mass and energy is particularly important since negative values would lead to non-physical results. The calculations for the transport of element centered variables (such as internal energy, the stress tensor, density and history variables) in LD is performed in accordance with the SALE3D strategy [16], and in this work using the Monotone Upwind Schemes for Conservation Laws (MUSCL) Van Leer scheme to achieve second order accurate monotonic results.

The fact that the velocities are located at the nodal points and not centered in the element (see Section 2.3), means that they must be advected separately. Furthermore, the momentum has to be conserved during this process and is a product of the element centered density and the nodal velocities. For the momentum transport, a more expensive method than SALE, the Half Index Shift (HIS) algorithm is used. This method was developed by D. J. Benson [17] in order to overcome the dispersion problems with the SALE strategy [13].

2.5 The Finite Volume Method formulation in OpenFOAM

The solver used in the OF simulations is an extension of the `icoFsiFoam` solver and uses an FV formulation for both the fluid and the structural solution of the coupled FSI analysis. The part of the FSI solver that handles the calculation of the *flow* is based on the standard OF solver `icoFoam`, which solves the incompressible laminar Navier-Stokes equations using the Pressure-Implicit Split-Operator (PISO) algorithm, while the mathematical description behind the *structural* solution procedure is based on an *updated* Lagrangian formulation.

2.5.1 Mathematical formulation of the fluid analysis

The mathematical description behind the fluid analysis in OF is based on the Eulerian differential approach for fluid flow described in Section 2.2.1. However, some assumptions and simplifications are made for the equations that are worth mentioning. First of all, any effects of gravity or other body forces are neglected throughout the entire analysis, making the body force vector disappear from the momentum equations. Secondly, the solver used in OF assumes that the fluid is incompressible. Hence the density is moved out of the convective term of equation (2.18), giving

$$\frac{\mathrm{d}\mathbf{v}}{\mathrm{d}t} = -\frac{1}{\rho}\nabla p + \nu\nabla^2\mathbf{v}. \tag{2.39}$$

where $\nu = \mu/\rho$ is the kinematic viscosity. Equations (2.39) are the incompressible Navier-Stokes equations that are solved in OF.

2.5.2 Mathematical formulation of the structural analysis

The majority of the changes in the extension of `icoFsiFoam` concerns the description of the solid phase. This is because the extended version is based on the *updated* Lagrangian

formulation and the mathematical description of this approach is thoroughly explained in the work done by Tuković and Jasak [18]. In order to provide a good insight to this formulation the main contents of their work is also included in this section.

The mathematical description of the structural analysis is based on the conservation principles introduced in Section 2.2. Moreover, solving flow problems in a deforming control volume requires a mathematical description of the relationship between the rate of change of the volume V and the motion of its surface, $\mathbf{v}_s$. This definition is called the *space conservation law* and is defined as

$$\frac{\mathrm{d}}{\mathrm{d}t}\int_V \mathrm{d}V - \oint_S \mathbf{n}\cdot\mathbf{v}_s \,\mathrm{d}S = 0 \tag{2.40}$$

Considering an isothermal continuum in an arbitrary volume V bounded by a surface S, the motion is hence governed by the conservation laws of mass and linear momentum, i.e:

$$\frac{\mathrm{d}}{\mathrm{d}t}\int_V \rho \,\mathrm{d}V + \oint_S \mathbf{n}\cdot\rho(\mathbf{v}-\mathbf{v}_s) \,\mathrm{d}S = 0 \tag{2.41}$$

$$\frac{\mathrm{d}}{\mathrm{d}t}\int_V \rho\mathbf{v} \,\mathrm{d}V + \oint_S \mathbf{n}\cdot\rho(\mathbf{v}-\mathbf{v}_s)\mathbf{v} \,\mathrm{d}S = \oint_S \boldsymbol{\sigma}\cdot\mathbf{n} \,\mathrm{d}S + \int_V \rho\mathbf{b} \,\mathrm{d}V \tag{2.42}$$

where $\mathbf{n}$ is the outward pointing unit normal to the surface S, $\mathbf{v}$ is the velocity of the continuum, $\mathbf{v}_s$ is the velocity of the surface S, $\boldsymbol{\sigma}$ is the Cauchy stress tensor and $\mathbf{b}$ is the resulting body force. The difference $\mathbf{v}-\mathbf{v}_s$ can be compared to the convective velocity $\mathbf{c}$ (equation (2.5)) discussed in Section 2.1, indicating that the mathematical formulation is in line with an ALE description taking into account the deforming mesh motion.

Assuming an elastic, isothermal structure the dynamic behavior can be described by considering only the linear momentum conservation law in Lagrangian formulation, i.e.

$$\frac{\mathrm{D}}{\mathrm{D}t}\int_V \rho\mathbf{v} \,\mathrm{d}V = \oint_S \boldsymbol{\sigma}\cdot\mathbf{n} \,\mathrm{d}S + \int_V \rho\mathbf{b} \,\mathrm{d}V \tag{2.43}$$

This can also be expressed in terms of the initial, undeformed control volume as

$$\int_{V_0} \rho_0 \frac{\partial\mathbf{v}}{\partial t} \,\mathrm{d}V_0 = \int_{S_0} (\mathbf{F}\cdot\boldsymbol{\Sigma})\cdot\mathbf{n}_0 \,\mathrm{d}S_0 + \int_{V_0} \rho_0\mathbf{b} \,\mathrm{d}V_0 \tag{2.44}$$

where the subscripts 0 denote quantities related to the initial, undeformed control volume, $\boldsymbol{\Sigma}$ is the second Piola-Kirchhoff stress tensor (see equation (2.21)) and $\mathbf{F}$ is the deformation gradient tensor (see Section 2.2.2).

Equation (2.44), which describes the *total* linear momentum conservation in Lagrangian formulation, can be written in an incremental form as

$$\int_{V_0} \rho_0 \frac{\partial\delta\mathbf{v}}{\partial t} \,\mathrm{d}V_0 = \int_{S_0} (\delta\mathbf{F}\cdot\boldsymbol{\Sigma} + \mathbf{F}\cdot\delta\boldsymbol{\Sigma})\cdot\mathbf{n}_0 \,\mathrm{d}S_0 + \int_{V_0} \rho_0\delta\mathbf{b} \,\mathrm{d}V_0 \tag{2.45}$$

where δ represents the increment of the corresponding variables and the deformation gradient tensor *increment* reads $\delta\mathbf{F} = (\nabla\delta\mathbf{u})$.

As previously mentioned, the mathematical approach is based on an *updated* Lagrangian formulation. This means that the reference configuration is continuously updated to (replicate) the latest calculated configuration. The corresponding *incremental* version of equation (2.22) becomes

$$\delta\boldsymbol{\Sigma} = 2G\delta\mathbf{E} + \lambda \,\mathrm{tr}\,(\delta\mathbf{E})\mathbf{I} \tag{2.46}$$

where $\delta\mathbf{E}$ is the increment of the Green-Lagrangian strain tensor for the *total* Lagrangian description and is defined as

$$\delta\mathbf{E} = \frac{1}{2}(\delta\mathbf{F}^{\mathrm{T}} \cdot \mathbf{F} + \mathbf{F}^{\mathrm{T}} \cdot \delta\mathbf{F}). \tag{2.47}$$

Finally, it appears that the linear momentum conservation equation for an elastic solid in the updated Lagrangian description, with the displacement vector increment $\delta\mathbf{u}$ as the primitive variable, can be obtained as:

$$\int_{V_u} \rho_u \frac{\partial \delta\mathbf{v}}{\partial t}\, \mathrm{d}V_u - \oint_{S_u} \mathbf{n}_u \cdot (2G + \lambda)\nabla\delta\mathbf{u}\, \mathrm{d}S_u = \oint_{S_u} \mathbf{n}_u \cdot \mathbf{q}\, \mathrm{d}S_u + \int_{V_u} \rho_u \delta\mathbf{b}\, \mathrm{d}V_u \tag{2.48}$$

where the subscript u corresponds to the updated variables and

$$\begin{aligned}\mathbf{q} = {} & G(\nabla\delta\mathbf{u})^{\mathrm{T}} + \lambda\,\mathrm{tr}\,(\delta\mathbf{u})\mathbf{I} - (G + \lambda)\nabla\delta\mathbf{u} + G\nabla\delta\mathbf{u} \cdot (\nabla\delta\mathbf{u})^{\mathrm{T}} \\ & + \frac{1}{2}\lambda(\nabla\delta\mathbf{u} : \nabla\delta\mathbf{u})\mathbf{I} + \boldsymbol{\Sigma}_u \cdot \delta\mathbf{u}_u^{\mathrm{T}} + \delta\boldsymbol{\Sigma}_u \cdot \delta\mathbf{F}_u^{\mathrm{T}}.\end{aligned} \tag{2.49}$$

The tensor $\mathbf{q}$ consists of nonlinear and coupling terms. In order to solve the discretized equation using a segregated algorithm, these terms are treated explicitly after the discretization. Jasak and Weller [19] claims that the efficiency of the segregated solution procedure can be improved by using the diffusivity $(2G + \lambda)$ in the Laplacian at the left-hand side of equation (2.48).

For a fully defined problem description the domain needs to be specified in both space and time, as well as being given proper initial and boundary conditions. The initial condition is simply the specified distribution of $\delta\mathbf{u}$ and $\delta\mathbf{v}$ at time zero, while there are several types of boundary conditions (which can be either constant or time-dependent); fixed displacement increment, plane of symmetry, fixed pressure increment, fixed traction increment and free surface.

The boundary conditions for fixed pressure increment and fixed traction increment are both implemented as a fixed normal derivative Neumann boundary condition on the displacement increment.

2.5.3 Solution procedure of the OpenFOAM solver

The analysis using the FV method requires a discretization of the computational domain in both time and space. The simulation time is split into a finite number of time steps, δt, and the discretized equations are solved in a stepwise manner, time step by time step. The computational space is discretized by splitting it into a finite number of control volumes.

The fluid and structural systems of equations are solved separately and sequentially for each time step. As previously mentioned, the solution of the flow field is calculated using the PISO algorithm; an iterative procedure for solving equations for velocity and pressure for transient problems [20]. The process is based on first evaluating initial guesses of the pressure and velocity fields using discretized equations of momentum[3] and then correcting them (at least) twice using a discretized *pressure correction equation* (derived from the equation of continuity). In this work, the discretization of the advection term (in OF) is done using the linear upwind scheme; a second-order extension of the standard upwind scheme [12]. Once the solution of the flow field has converged the pressure and shear

[3]There are several numerical schemes available to discretize the momentum equations. The details about these schemes are extensive and hence not provided in this report, but can be found in e.g. Versteeg & Malalasekera [12].

stresses are assembled into the traction vector. As described in Section 2.3 the traction is then introduced into the structural equations. The following numerical evaluation of the structural displacements is similarly obtained by solving the system of discretized linear momentum conservation equations for an elastic solid in the updated Lagrangian description. Finally, the fluid and structural meshes are both moved in accordance with the calculated displacements. The steps of the solution procedure can be summarized as follows:

1. Guess velocity and pressure fields
2. Evaluate the guesses of velocity and pressure and correct them until convergence

   i) Extract traction vector from the converged flow equation system

   ii) Introduce traction vector into structural equations
3. Evaluate the incremental displacements of the structure
4. Move meshes in accordance with structural displacements

   i) Extract incremental displacement velocity from the structural solution

   ii) Introduce incremental displacement velocity into flow equations

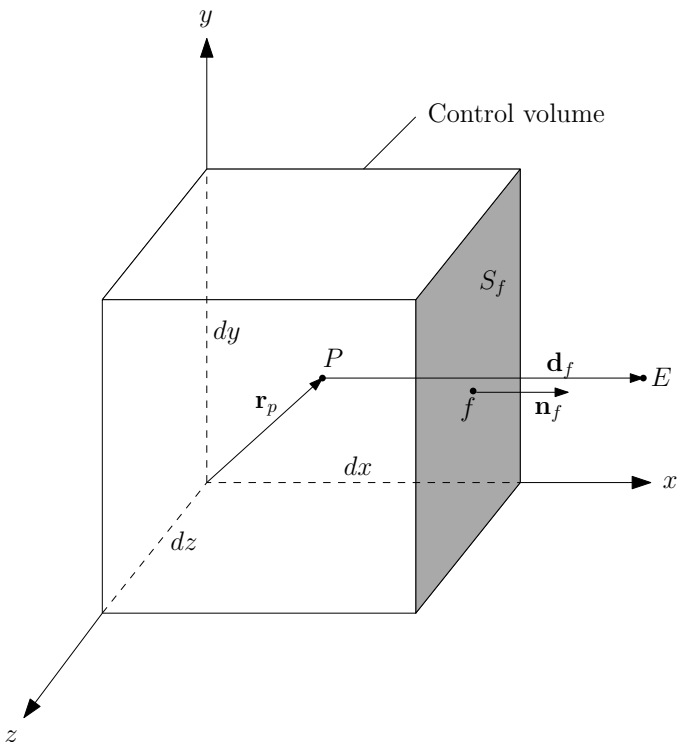

Figure 2.8: Hexahedral control volume.

Figure 2.8 shows an example of a hexahedral control volume around the computational point P located in the center of the control volume, its face f, its face area S_f, the face unit normal vector $\mathbf{n}_f$ and the center point E of the neighboring control volume sharing the face f.

Since the conservation of linear momentum is described by the incremental updated Lagrangian formulation (equation (2.48)), the computational mesh has to be moved at the beginning of each time step. This is done by using the displacement increment vector

obtained from the previous time step. The cell-centered FV method that is used in OF calculates the displacement increment at the control volume center. Thus the calculated displacement increment must be interpolated onto the control volume vertices to enable the dynamic mesh movement. This interpolation is done using a weighted averaging interpolation given by

$$\delta\mathbf{u}_p = \frac{\sum_c w_{pc}\left[\delta\mathbf{u}_c + (\mathbf{r}_p - \mathbf{r}_c)\cdot(\nabla\delta\mathbf{u})_c + \frac{1}{2}(\mathbf{r}_p - \mathbf{r}_c)^2{:}(\nabla\nabla\delta\mathbf{u})_c\right]}{\sum_c w_{pc}}, \tag{2.50}$$

where $\delta\mathbf{u}_p$ is the displacement increment of vertex p and $\delta\mathbf{r}_c$ denotes the displacement increment at the center of the control volume. The summation is done over all control volumes sharing the p vertex and the weighting factor w_{pc} is defined as

$$w_{pc} = \frac{1}{|\mathbf{r}_p - \mathbf{r}_c|}, \tag{2.51}$$

where $\mathbf{r}_c$ denotes the position vector of the control volume center and $\mathbf{r}_p$ is the position vector of the vertex p.

3 Simulation setups

As stated in Section 1.3, the computational work consists of two parallel studies which are performed using OF and LD. Due to the different numerical approaches the domains have to differ in some aspects. The following section presents the different setups (e.g. domains, boundary conditions etc.) for the different analyses.

3.1 Material properties

As indicated in Section 1.3 and 1.4 the fluid medium used in the simulations is water. Some properties of interest of water at 20°C are listed in Table 3.1.

Table 3.1: Some properties of water at room temperature (20°C) [21, 22].

Density (ρ)	Dynamic viscosity (μ)	Kinematic viscosity (ν)	Speed of sound (v_{sound})
998.2 [kg/m^3]	$1.005 \cdot 10^{-3}$ [kg/(m·s)]	$1.004 \cdot 10^{-6}$ [m^2/s]	1492 [m/s]

The value for speed of sound is used to calculate the bulk modulus (K) of water. The bulk modulus describes a material's resistance to undergo compression, i.e. a high bulk modulus relates to a low compressibility. The speed of sound can be related to the bulk modulus as [23]

$$v_{sound} = \sqrt{\frac{K}{\rho}} \tag{3.1}$$

and hence the bulk modulus of water at 20°C becomes

$$K = \rho v_{sound}^2 \approx 2.2 \cdot 10^9 \text{ [Pa]}. \tag{3.2}$$

The solver used in LD does not assume an incompressible fluid (as opposed to the solver used in OF). Thus, in order to omit compressibility a bulk modulus is needed to explicitly command the LD solver to treat water as an incompressible fluid. Unfortunately, a bulk modulus as high as in (3.2) results in extensive calculation times. Hence the assumption is made that a bulk modulus of the magnitude 10^6 is adequate to avoid any compressibility effects in LD.

The material properties for the EVG are more troublesome to determine. No such information is available from the manufacturer. Hence, the material properties has to be extracted and approximated via literature from similar studies. Two such studies were performed by Li and Kleinstreuer [1, 6] from which the properties of the EVG material in the present study are extracted. These are summarized in Table 3.2.

Table 3.2: Material properties of the EVG.

Thickness (h)	Young's modulus (E)	Poisson's ratio (η)	Density (ρ)
0.003 [m]	10 [MPa]	0.27 [-]	6000 [kg/m^3]

3.2 Laminar flow in a rigid pipe

To evaluate the two software modules ability to simulate a flow field, a study of a straight, *rigid* cylindrical pipe subjected to a steady, laminar flow of water is conducted. To gain further confidence in the simulations, the results of the study are validated against the analytical solution for a laminar fully developed pipe flow (see Appendix A).

3.2.1 Geometry

The analysis is performed on a straight, rigid pipe with diameter $d = 0.014$ m, i.e. the same diameter as the subsequently analyzed EVG. The length of the pipe is chosen due to the requirement that the flow has to be fully developed for a certain interval of the pipe length. This requirement has to be fulfilled in order to compare the simulations with the analytical solution for a *laminar* fully developed pipe flow. According to [10], the pipe length needed for the flow to reach a fully developed profile, L_e, can be related to the pipe diameter, d, and the Reynolds number, Re_d, as

$$L_e \approx 0.06 d \mathrm{Re}_d. \tag{3.3}$$

The commonly accepted design value for pipe flow transition from laminar to turbulent flow is [10]

$$\mathrm{Re}_{d,crit} \approx 2300. \tag{3.4}$$

In order to ensure a laminar flow, the inlet velocity condition for the simulations is chosen to be $v = 0.12$ m/s. Considering water (at room temperature) as the fluid medium, this give a Reynolds number of

$$\mathrm{Re}_d = \frac{vd}{\nu} \approx 1673. \tag{3.5}$$

According to equation 3.3 this requires a pipe length, L_e, of approximately 1.4 meters for the flow to reach a fully developed profile. To enable a comparison with the analytical solution the pipe length was set to 2 meters.

3.2.2 Mesh

To save computational time, the simulation is done for half the pipe by making use of symmetry the same way as for the final EVG case. The mesh topology used is an *o-grid* which is commonly used for pipe flow simulations thanks to its capability of resolving the boundary layer, see Figure 3.1a. The flow is simulated using the FSI solvers (in *uncoupled* mode). This is because the main reason of the analysis is to compare the solvers and the way they solve the flow field.

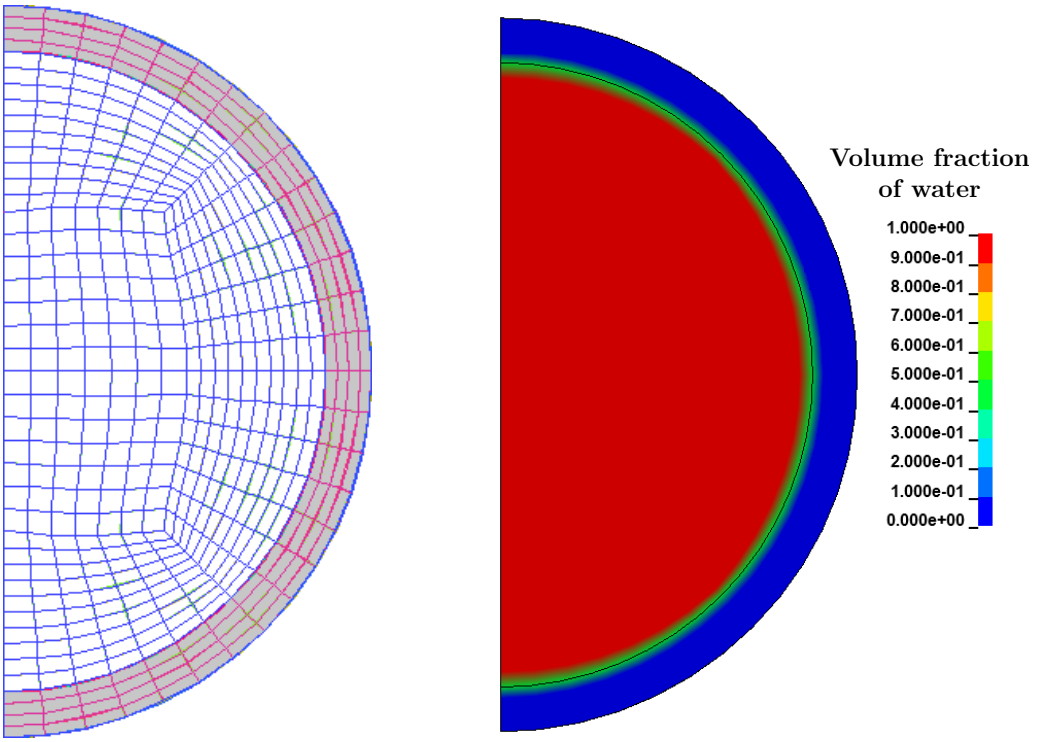

(a) (b)

Figure 3.1: Cross-section of the fluid *and* structural mesh used in OF, but *also* the Eulerian mesh used in LD. In (a) white segment denotes the fluid domain containing water and the shaded segment denotes the structural mesh in OF *or* the outer Eulerian mesh in LD. In (b) the volume fraction of water in LD is seen.

In OF the FV approach requires the structural mesh to be three-dimensional, i.e. it had to consist of volume elements. In LD, however, the ALE approach allows for shell elements to be used for the structure. Moreover, the ALE formulation (used in LD) necessitates for the Lagrangian (i.e. structural) mesh to be fully enclosed by the Eulerian (i.e. fluid) mesh. This is partly because the Lagrangian-Eulerian interfaces are not allowed to share nodes (as opposed to the fluid-structure interface in OF). Consequently, the Eulerian mesh has to exceed the structural geometry to prevent any possible voids between the Lagrangian and Eulerian meshes, so that the interface reconstruction (see Section 2.4.2) can function properly. Furthermore, the subsequent coupled FSI analysis is based on the MMALE formulation. This means that the Eulerian domain has to consist of (at least) two different materials; in this case water (inside the EVG) and a dummy material, given the density of air (outside the EVG), see Figure 3.1b. This further calls for the Eulerian mesh to fully enclose the structural geometry. An initialization of the volume fractions (see Appendix C) with the structural geometry as container is made to further ensure the correct material distribution.

Conveniently, the outer part of the Eulerian mesh in LD is used as the structural mesh in OF (or vice versa). The final mesh is made up entirely of hexahedrons and is generated using ANSYS ICEM CFD, giving a total cell count of $734,510$.

3.2.3 Boundary conditions

The boundary conditions for the rigid pipe simulation are summed up in Table 3.3.

Table 3.3: Boundary conditions for the rigid, straight pipe simulation.

Boundary	**Type**	**Value**
Inlet	Steady, uniform velocity	0.12 [m/s]
Outlet	Mean pressure	0 [Pa]
Wall	No-slip	0 [m/s]
Symmetry plane	Symmetry	-

3.3 Coupled analysis of the EVG

The coupled FSI analysis is performed using two different flow scenarios; first off a steady flow with 0.5 m/s uniformly distributed across the inlet, followed by a pulsating, sinusoidal flow fluctuating from 0 to 1 m/s. The frequency of the sinusoidal flow corresponds to a heart rate of 60 bpm.

3.3.1 Geometry

The pipe is given the diameter $d = 0.014$ meters and the length $L = 0.160$ meters (see Figure 3.2). The pipe is also given a predefined angle between the inlet and outlet normal vectors. Since this angle[4] is dependent on, for example, the specific patients anatomy and the shape of the aortic aneurysm, there is no preferred angle from a medical point of view. Thus the angle is set to 90 degrees.

The computational domains are extended with straight inlet and outlet regions before and after the EVG. The reason for having an inlet extension is mainly to allow for the flow to develop a boundary layer before entering the flexible EVG. The purpose of the outlet extension is to minimize the effects from the prescribed pressure at the outlet. Ideally, these extensions would be infinitely long. However, to ensure reasonable calculation times the lengths of the extensions has to be limited. Accordingly, the extensions are both given the length $l_{i,o} = L/2 = 0.08$ meters.

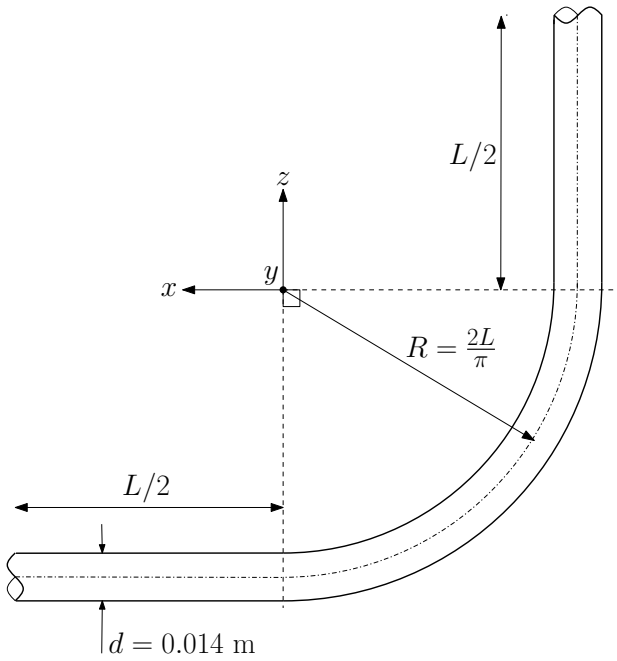

Figure 3.2: The geometry of the setup.

[4] i.e. angle of a surgically inserted stent graft

3.3.2 Mesh

The simulations for the two software modules are performed on two different mesh setups. In LD a cartesian Eulerian mesh is used, divided into two parts (see Figure 3.3) enabling the definition of two different materials.

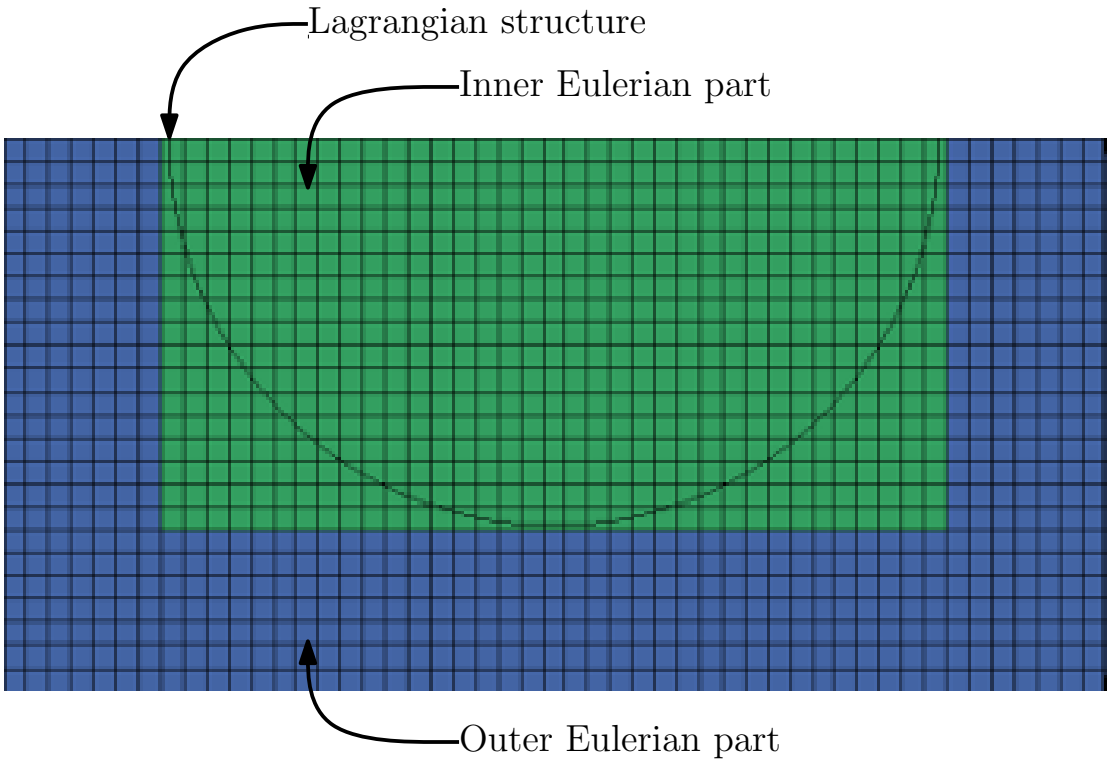

Figure 3.3: The fluid and structural meshes used in LD.

The initialization (as described in Section 3.2.2) of the volume fractions for the two materials, recently associated with the mesh, is made such that water is enclosed by the Lagrangian structure, with the dummy material surrounding it (see Figure 3.4).

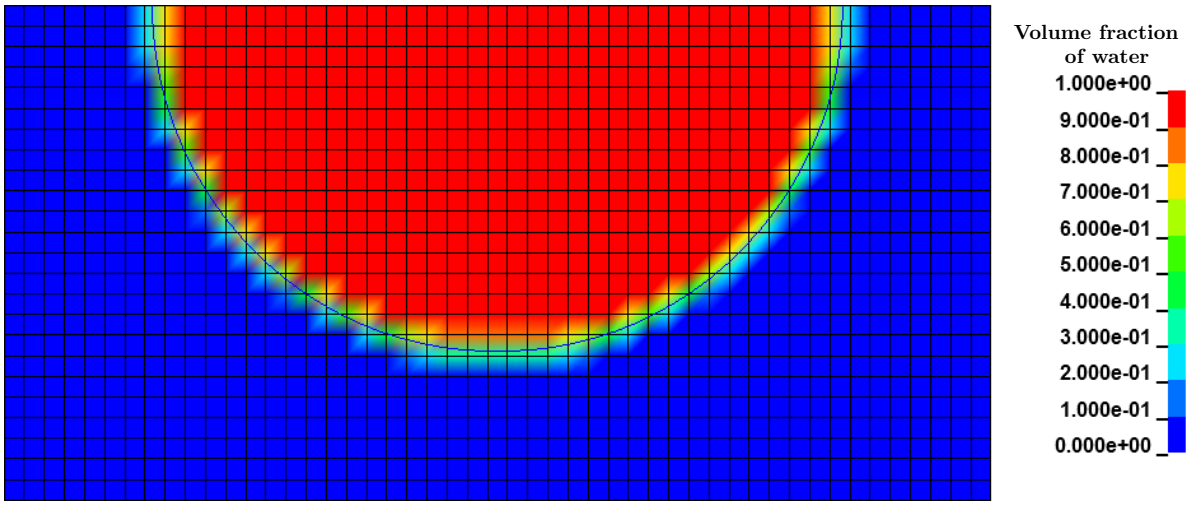

Figure 3.4: The initial volume fraction of water at $t = 0$.

The OF mesh (see Figure 3.5) differs drastically from the LD mesh (see Figure 3.6). In OF the flow is resolved using an o-grid. Once again, the requirement of using volume

elements in OF necessitates a certain thickness of material for the structure. Since the structural solver in OF is highly unstable for very thin walls the structure is given a thickness of 3 millimeters, which is made up by a layer of additional cells surrounding the o-grid.

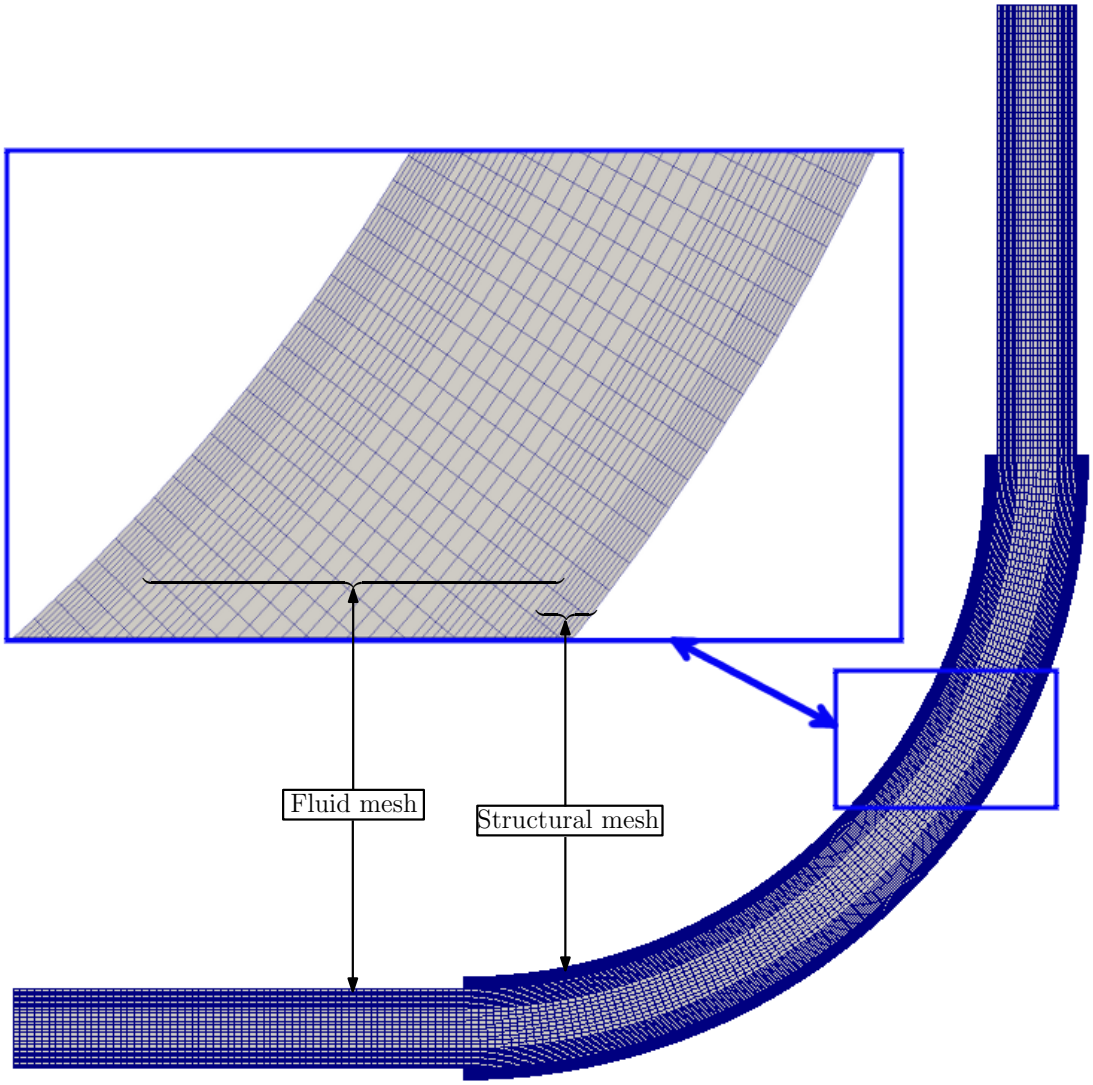

Figure 3.5: The fluid and structural meshes used in OF.

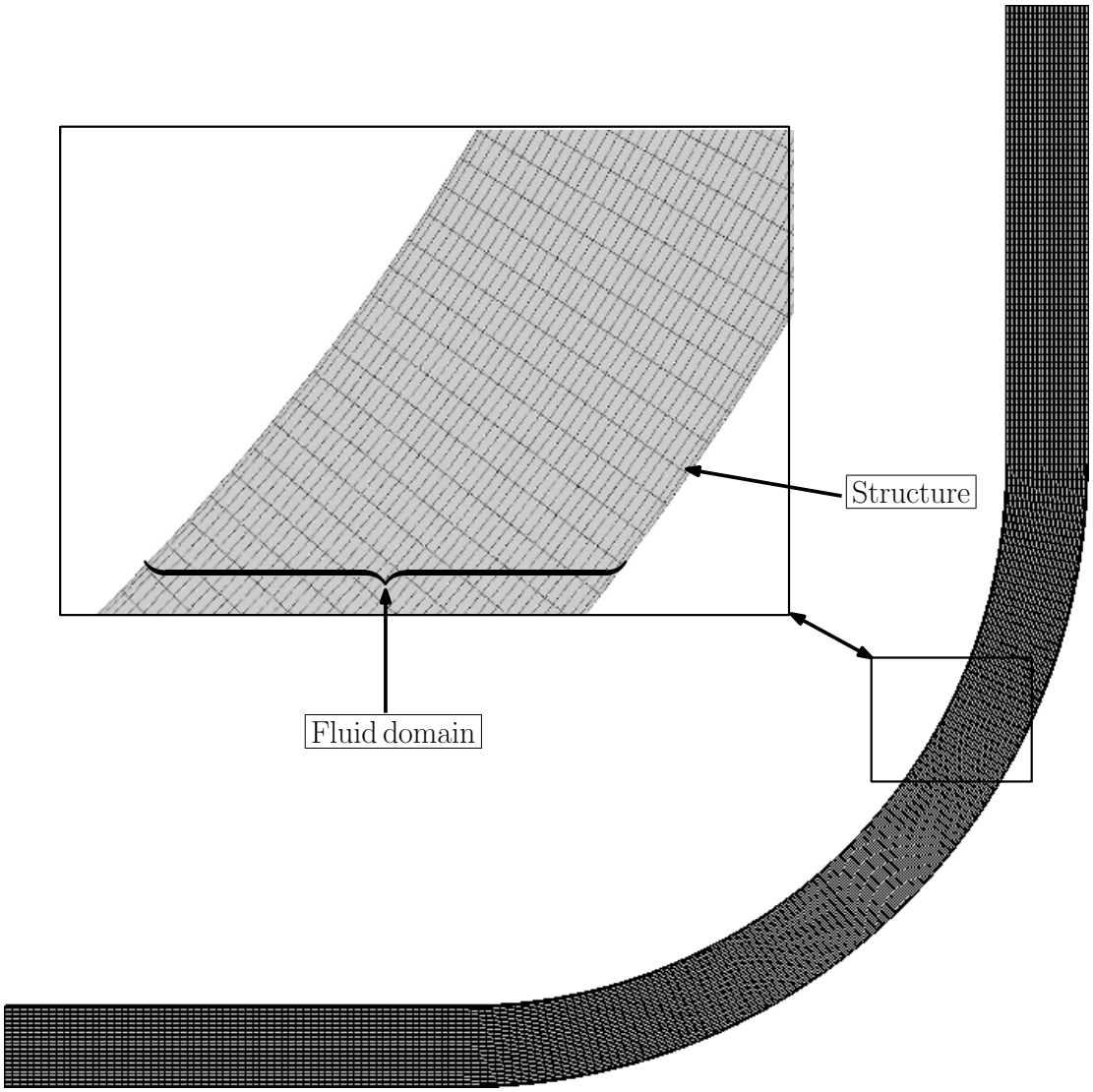

Figure 3.6: The inner Eulerian (fluid) mesh and the structural mesh used in LD.

Additionally, the numerical approach in OF makes it possible to set a wall no-slip condition directly on the fluid mesh at the inlet and outlet extensions. This makes it possible to define a structural domain only for the bend (see Figure 3.7), which consequently reduces the calculation time. On the other hand, the MMALE approach used in LD requires for the structure to stretch through the entire Eulerian domain. This is necessary in order to numerically separate the two materials and reconstruct the interface.

The final meshes in OF are made up entirely of hexahedrons and have a total cell count of $108,360$. The LD meshes consist of a total of $285,768$ fluid (hexahedral) elements and $13,616$ structural (shell) elements. All meshes are generated using ANSYS ICEM CFD.

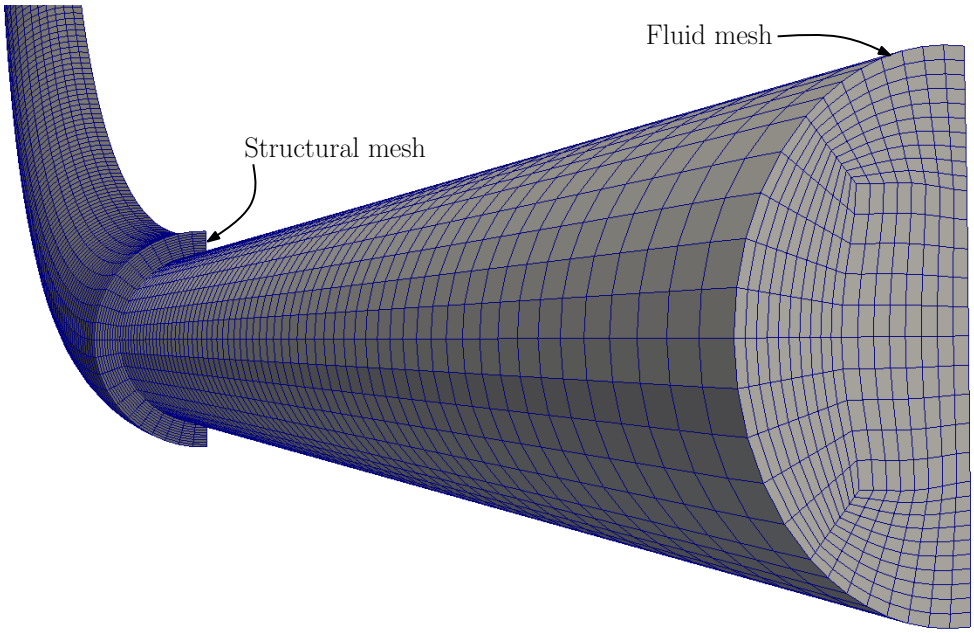

Figure 3.7: The fluid and structural meshes used in OF.

3.3.3 Boundary conditions

The boundary conditions used in the coupled analysis are summed up in Table 3.4. The inlet boundary has been given two different conditions corresponding to the steady-state flow and the pulsating flow, respectively.

Table 3.4: Boundary conditions for the coupled analysis.

Software	**Boundary**	**Type**	**Value**
OF	Inlet	Steady-state velocity	0.5 [m/s]
		Periodic velocity	$0.5 + 0.5sin(2\pi ft)$ [m/s]
	Outlet	Mean pressure	0 [Pa]
	Rigid walls	No-slip	-
	Flexible walls	Moving wall velocity	-
	Symmetry plane	Symmetry	-
LD	Inlet	Steady-state velocity	0.5 [m/s]
		Periodic velocity	$0.5 + 0.5sin(2\pi ft)$ [m/s]
	Outlet	Zero traction	0 [N/m^2]
	Rigid walls	No-slip	-
	Flexible walls	Moving wall velocity	-
	Symmetry plane	Symmetry	-

4 Results

This section covers the results of both the LD and the OF simulations. The simulations consist of three groups: firstly the flow solution comparison for a straight rigid pipe, secondly a steady flow through the bent EVG and finally a pulsating flow through the bent EVG. Pressure and velocity distribution at selected locations (see Figure 4.1) as well as normal forces at the upstream and downstream attachments of the EVG are presented.

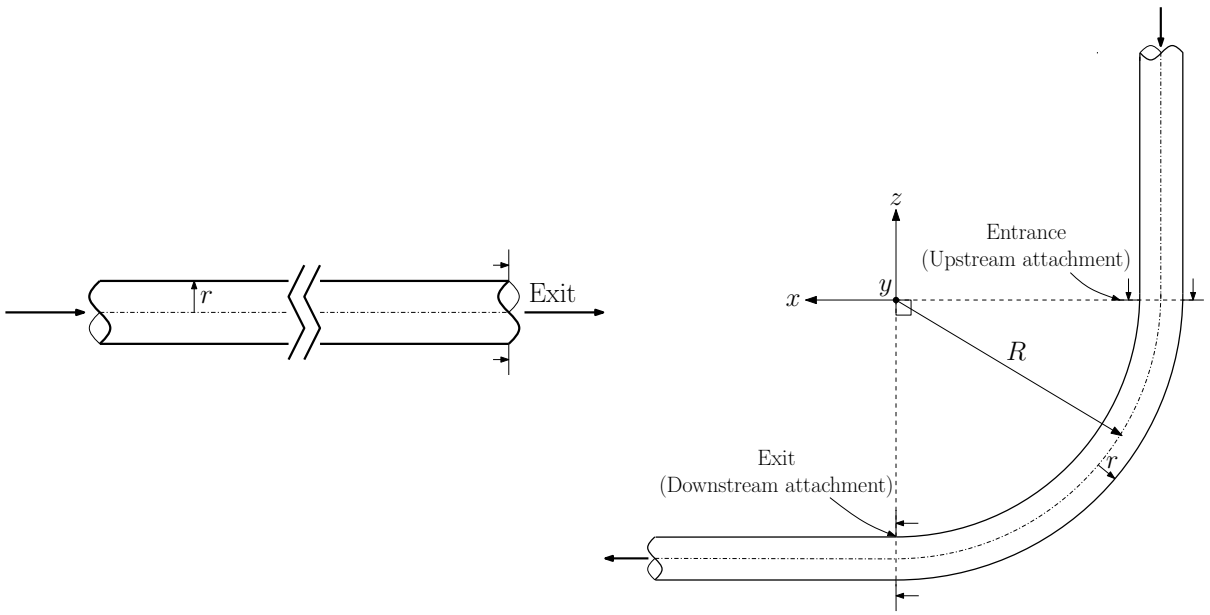

(a) Straight setup (b) Bent EVG setup

Figure 4.1: Setup overviews. Pressure and velocity cross-section profiles extracted at "Entrance" and "Exit" and normal forces in the coupled analysis extracted at the upstream and downstream attachments, respectively.

4.1 Validation of laminar flow in a rigid pipe

The data from the straight rigid pipe simulations are sampled at the outlet (or "Exit", see Figure 4.1a) cross-section, after a simulated time of 14 seconds. At this point the flow is considered to be fully developed for both solvers. Figure 4.2a shows the cross-section velocity profiles for OF, LD and the analytical solution (see Appendix A). The cross-section pressure profiles for OF and LD is plotted in Figure 4.2b.

For the OF simulation the velocity profiles at the outlet show great correspondence with the analytical solution. The LD simulation seems to give a generally lower velocity than both OF and the analytical solution, with the exception of the near wall regions (i.e. $-0.007\text{ m} < r \leq -0.006\text{ m}$ and $0.006\text{ m} \leq r < 0.007\text{ m}$).

For the pressure (see Figure 4.2b) some characteristic similarities can be seen between the OF and LD results. However, the pressure at the outlet is lower in LD (though only with 0.01 Pa) and shows a more distinct variation of pressure across the pipe. Recall that the outlet boundary condition in OF was set to a mean pressure of 0 Pa (see Section 3.2). If assembling the OF pressure in Figure 4.2b, the mean value is not 0 Pa. This is because the pressure from the OF simulation is sampled in the cell-centers (i.e. slightly upstream of the outlet boundary), while the pressure from the LD simulation is sampled directly on the boundary. This most certainly contributes to the differences in pressure. Moreover, OF solves for an incompressible flow while LD solves for a compressible fluid with a high bulk

modulus. This ought to further contribute to the differences for the pressure calculation.

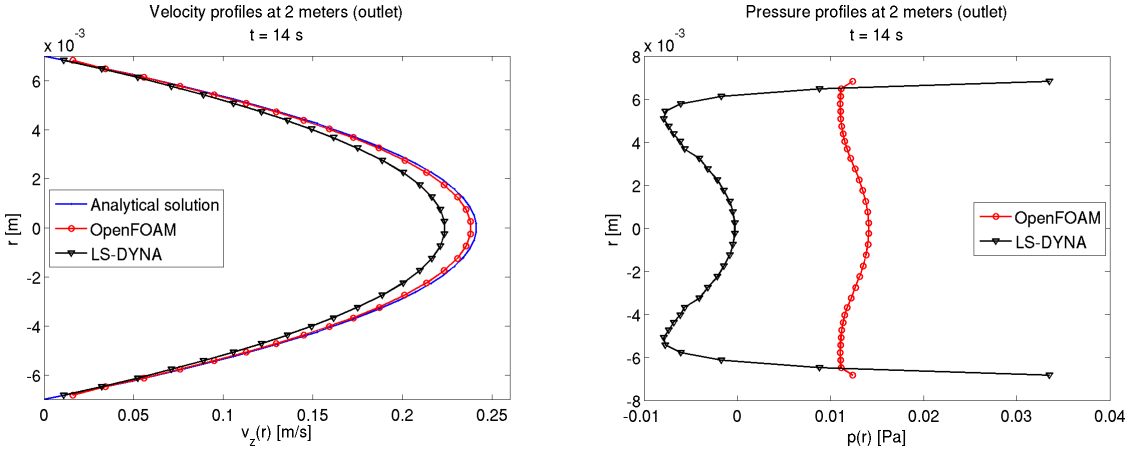

(a) (b)

Figure 4.2: Plots showing a) velocity profiles of analytical solution, OF simulation and LD simulation and b) pressure profiles of OF simulation and LD simulation.

4.2 Steady flow with FSI

This section presents the results from the simulations using a steady inlet flow boundary condition with the velocity 0.5 m/s, also taking into account the coupling between the fluid flow and the structure. Figure 4.3 shows comparisons of the cross-sectional velocity and pressure profiles in the symmetry plane. The profiles in Figure 4.3a and Figure 4.3c are extracted at the entrance of the bent EVG (i.e. upstream) and the profiles in Figure 4.3b and Figure 4.3d at the exit of the bent EVG (i.e. downstream).

The pressure and velocity profiles from the two softwares are plotted at different times, i.e. $t = 2$ s for LD and $t = 3$ s for OF. This is because the LD simulation is run with activated coupling from $t = 0$ s, while the coupling in OF is not activated until the flow has been stabilized (e.g. at $t = 2$ s). The reason for this is the OF solver's sensitivity to the large, transient forces that occur during the development of the flow field. An example of such large force transients, extracted from the LD simulation, can be seen in Figure 4.5a.

Figure 4.4 shows the velocity and pressure fields in the symmetry plane obtained at $t = 2$ s (LD) and $t = 3$ s (OF), respectively. Figure 4.5c and Figure 4.5d show comparisons of the normal forces in the upstream and downstream attachments of the bent EVG for the last 0.5 s of each simulation. As can be seen in Figure 4.5b, the structure in the OF simulation still experience a "shock" when the coupling is activated, requiring some time for the forces to stabilize. However, the magnitudes of these force transients are much lower than those experienced when activating the coupling already from $t = 0$ s.

The velocity results for OF and LD (see Figure 4.3) show that the flow is not fully developed before entering the EVG, although a boundary layer is starting to develop. The boundary layer seems to be further developed in OF than in LD, yielding velocity peaks near the walls in the LD velocity profile. The reason for the less developed boundary layer in LD is most certainly due to the lower mesh density close to the walls (in comparison with the mesh in used in OF).

For both softwares there is a slightly higher velocity towards the leftmost wall (i.e. -0.006 m $< r < -0.003$ m). This makes sense since the flow is forced by the pressure gradient to "turn" into the bent EVG, causing the flow to accelerate in this region. This is further validated by the pressure profiles in Figure 4.3c. It should be noted that the

volume fraction method used in LD (see Section 2.4.2) creates uncertainties regarding the accurateness of the near wall solution variables. Even though the velocities are of similar magnitude here, the impact of the transition region between the dummy material and the water can not be disregarded. Furthermore, severe leakage of the water into the outer domain (see Figure 4.6) occur at the inlet boundary as well as local pressure and velocity peaks. This affects the whole solution and is most probably the reason for the large differences between the two solver simulations. Hence, the velocity and pressure profiles for OF and LD, in this section, show less correspondence than the results from the validation of laminar flow in a rigid pipe (see Section 4.1).

The acceleration near the leftmost wall causes the flow to separate when entering the EVG (as clearly indicated in Figure 4.4a and 4.4b). The separation gives rise to a large decrease in pressure near the innermost wall (see Figure 4.3d and Figure 4.4c - 4.4d). Worth noting is that Figure 4.4a indicates that the flow field is laminar, while Figure 4.4b implies occurence of turbulence. This partly originates from the use of different meshes, but also from the use of different numerical advection schemes in the two softwares. The presence of turbulence in LD is further indicated by the randomness of the velocity profile at the exit of the EVG (see Figure 4.3b).

When further comparing the pressure profiles at the entrance and exit of the EVG (Figure 4.3c and 4.3d) it is evident that the pressure drop through the pipe is larger in LD than in OF. This is, again, validated by the pressure fields in Figure 4.4c and 4.4d. Consequently, the velocities are somewhat higher in the LD simulations, as well as the normal forces in both the upstream and downstream attachments (see Figure 4.5). The different coupling methods may contribute to these differences, even though their impact is probably lesser than the two softwares' ways of solving the flow field. Moreover, in both solvers the normal force in the upstream attachment is larger than the downstream normal force. This is likely to originate from the separation of the flow, yielding a steep pressure gradient in the lower half of the EVG (see e.g. Figure 4.7e).

From the momentum balance calculations, (see Appendix B) a rough estimate is given for the upstream and downstream forces where $F_x = F_y \approx 0.03841$ N. For OF the upstream force fluctuates around 0.0375 N and for LD around 0.0625 N. The downstream force for OF fluctuates around 0.0315 N and LD around 0.0465 N. For both forces, OF is slightly lower than the estimates. This is due to the calculations being performed for a streamtube where the streamlines are the same throughout the tube and no losses are considered. In the EVG there are frictional losses which reduces the force acting on the structure. For LD the forces are higher than the estimated forces, in line with previously discussed pressure and leakage related reasons.

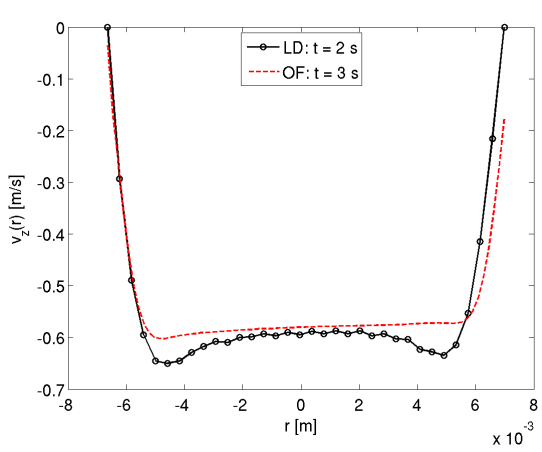

(a) Entrance velocity profiles

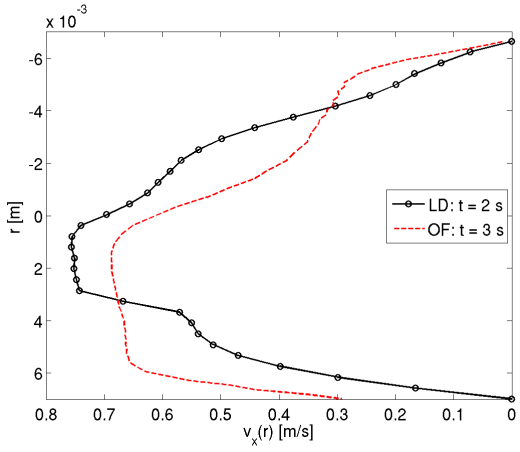

(b) Exit velocity profiles

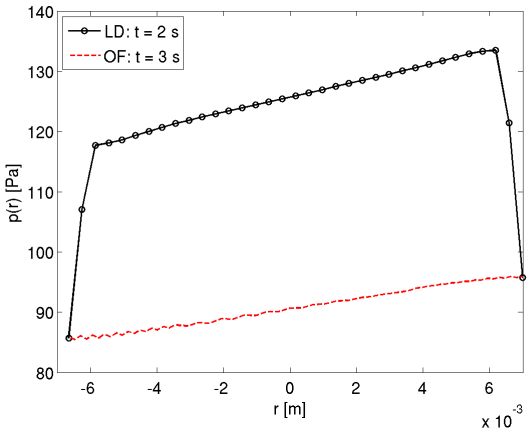

(c) Entrance pressure profiles

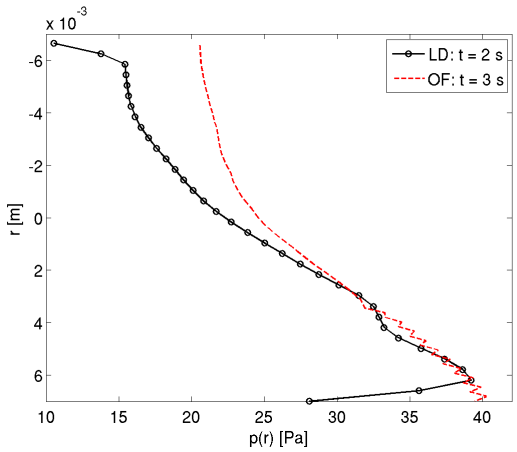

(d) Exit pressure profiles

Figure 4.3: Plots showing b,c) cross-section velocity profiles and d,e) cross-section pressure profiles at the entrance and exit of the bent EVG at $t = 2$ s (LD) and $t = 3$ s (OF). Inlet velocity: $v_z = -0.5$ m/s.

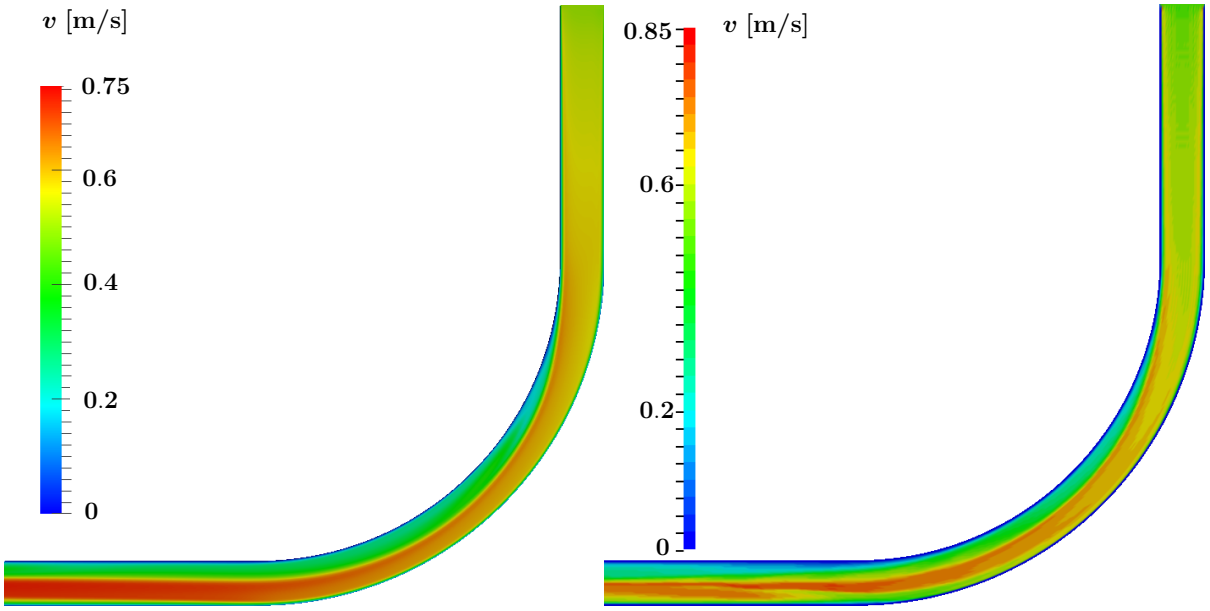

(a) Velocity field, OF ($t = 3$ s)

(b) Velocity field, LD ($t = 2$ s)

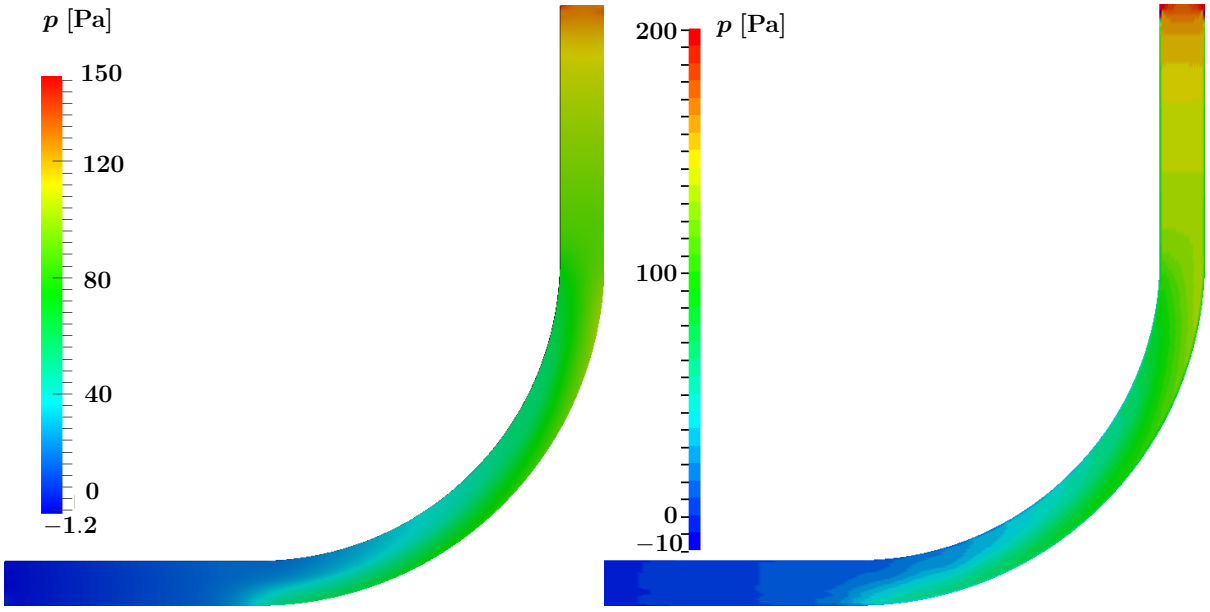

(c) Pressure field, OF ($t = 3$ s)

(d) Pressure field, LD ($t = 2$ s)

Figure 4.4: a,b) showing velocity fields and c,d) showing pressure fields for OF and LD respectively.

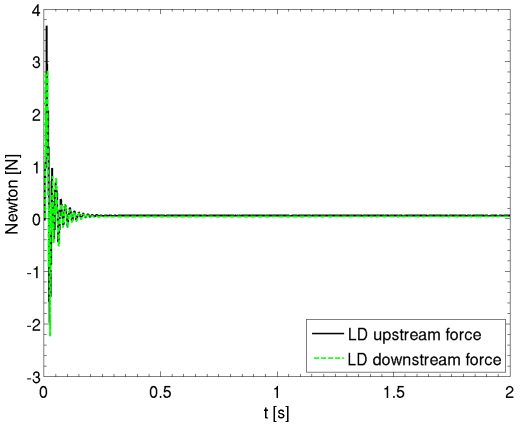

(a) Normal forces (LD)

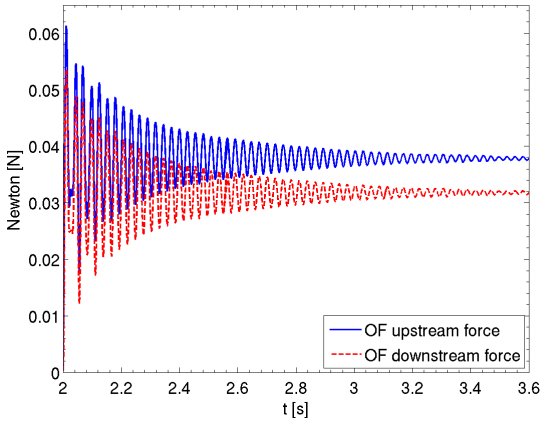

(b) Normal forces (OF)

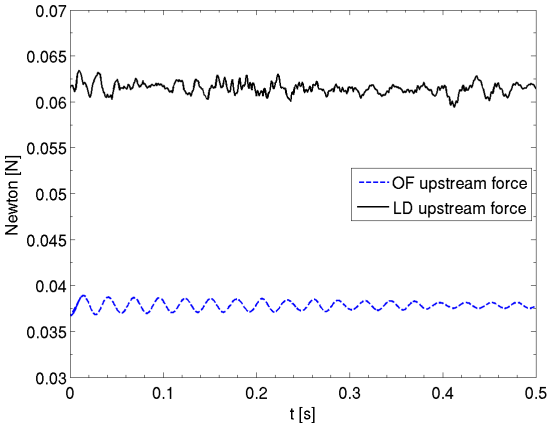

(c) Upstream attachment, last 0.5 s (OF, LD)

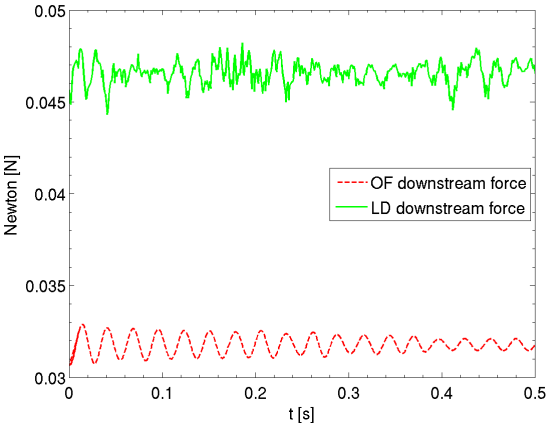

(d) Downstream attachment, last 0.5 s (OF, LD)

Figure 4.5: Plots a,b) showing force transients and c,d) showing comparisons of normal forces at upstream and downstream attachments for the last 0.5 s, respectively.

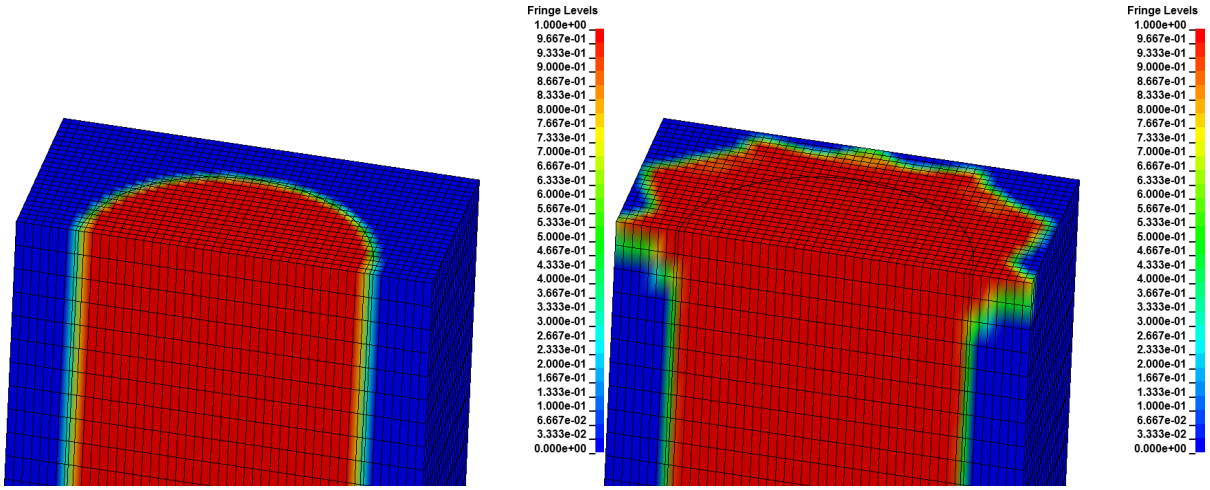

(a) Volume fraction $t = 0$ s

(b) Volume fraction $t = 0.1$ s

Figure 4.6: a) showing initial volume fraction and b) the volume fraction after 0.1 s, illustrating the leakage for the steady flow case in LD.

4.3 Pulsating flow with FSI

This section presents the results from the simulations using a sinusoidal velocity inlet flow boundary condition. The velocity and pressure results are presented at five different times and at each time the results are accompanied by a plot showing the current stage of the inlet pulse. Figure 4.7-4.11 show the velocity and pressure fields in the symmetry plane at five different stages of the inlet pulse. The reason for the different sampling times is again the OF solver's sensitivity to the initial force instabilities (see Section 4.2). Figure 4.12 - 4.16 show velocity and pressure fields in the symmetry plane at five different stages of the sinusoidal inlet flow condition.

Figure 4.17 shows comparisons of the normal forces in the upstream and downstream attachments of the EVG. The forces extracted from LD are sampled from $t = 0$ s, including the initial instabilities. This is not the case for OF where the simulation is split into three stages (see Appendix D) due to the solver sensitivity. Hence the normal forces are extracted and plotted only for the last stage, when the forces have been stabilized.

In Figure 4.7 and 4.8 it can be seen that the first 0.5 seconds of the sampled pulses show great similarities with the profiles from the simulations using a steady inlet flow condition (see Section 4.2). This is the case also for the last sampling point (see Figure 4.11). As for the steady flow simulation, the flow characteristics correspond fairly well between the two numerical solutions, though the magnitudes of pressure and velocity deviate here as well. This is most likely due to the inlet boundary leakage in LD (see Figure 4.18), discussed in Section 4.2.

The greatest differences between the solvers occur when approaching zero inlet velocity, hence between 0.5 s $\leq t \leq$ 1 s (see Figure 4.8 - 4.10 and 4.13 - 4.15). The decreasing inlet velocity induces turbulence and since using different grids and advection schemes, the turbulence is not resolved equally. The two advection schemes handle the flux over each cell differently, leading to a deviation in transport of the solution variables. Since neither of the grids are fine enough to fully resolve the smallest scales, none of the solutions can. in this sense, be said to be more accurate. However, OF offers a finer mesh close to the structure, yielding a better resolved boundary layer. Nonetheless, the results within this interval must be considered more uncertain.

The normal forces (see Figure 4.17) show fair correspondence with the sinusoidal inlet pulse, though the forces are not entirely sinusoidal. What may be noted is the phase shift of the forces in comparison to the sinusoidal inlet velocity, i.e. the forces reach their critical values before the inlet velocity, but to clarify the reasons for this behavior more extensive simulations are required. Again, as for the steady state analysis, the forces are consistently larger in LD than in OF, and the force at the upstream attachment is generally larger than the downstream force in both solvers. Also, the tugging (i.e. positive) forces that arise from the stretching of the EVG are slightly larger than the compressive (i.e. negative) forces that arise when the structure retracts from a stretched state.

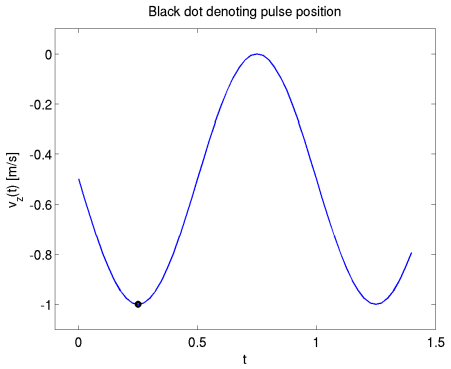

(a) Stage of inlet pulse (denoted by •)

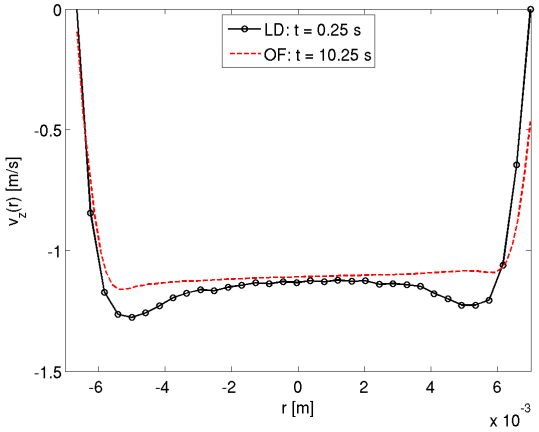

(b) Entrance velocity profiles

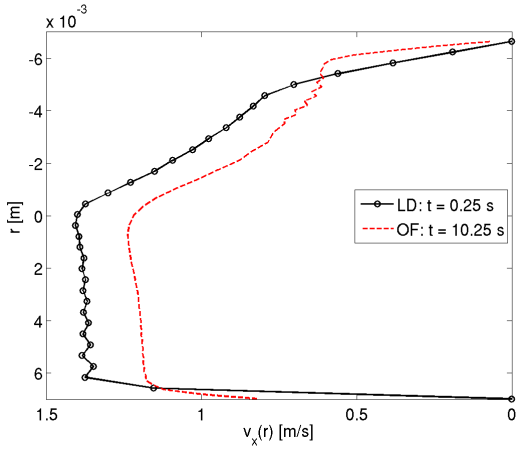

(c) Exit velocity profiles

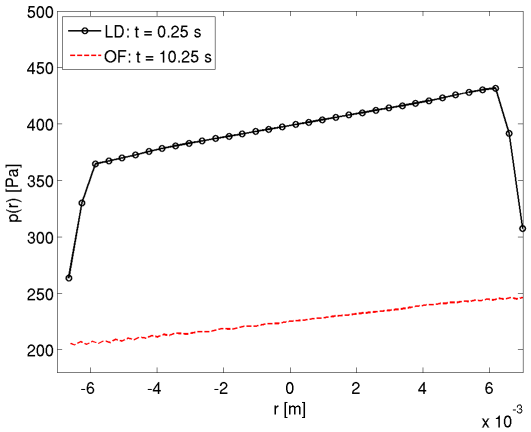

(d) Entrance pressure profiles

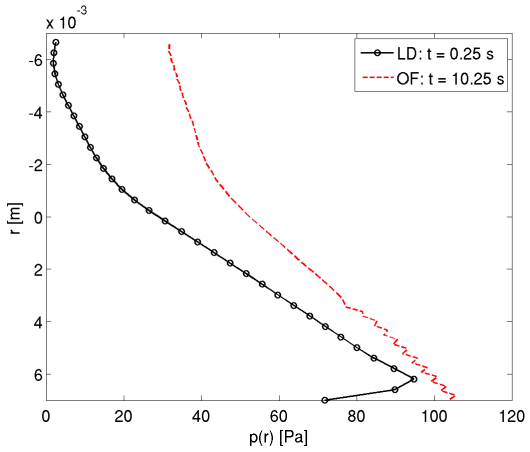

(e) Exit pressure profiles

Figure 4.7: Plots showing a) the stage of the inlet pulse, b,c) cross-section velocity profiles and d,e) cross-section pressure profiles at the entrance and exit of the bent EVG. Inlet velocity: $v_z = -1$ m/s.

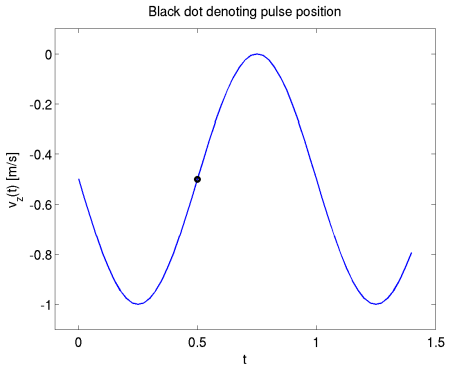

(a) Stage of inlet pulse (denoted by •)

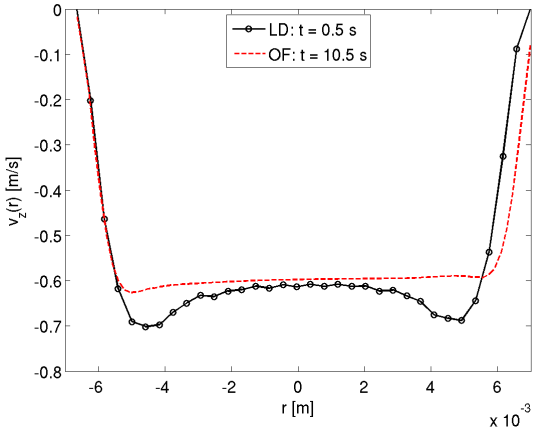

(b) Entrance velocity profiles

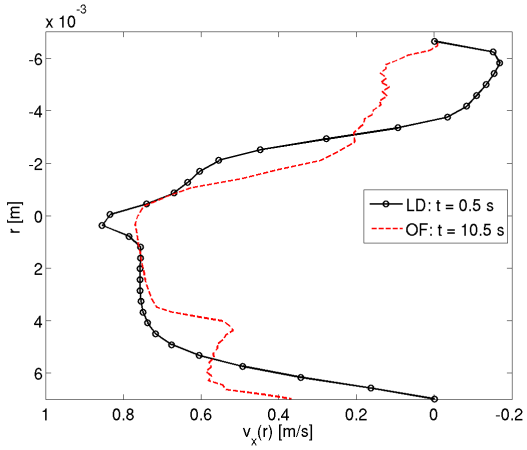

(c) Exit velocity profiles

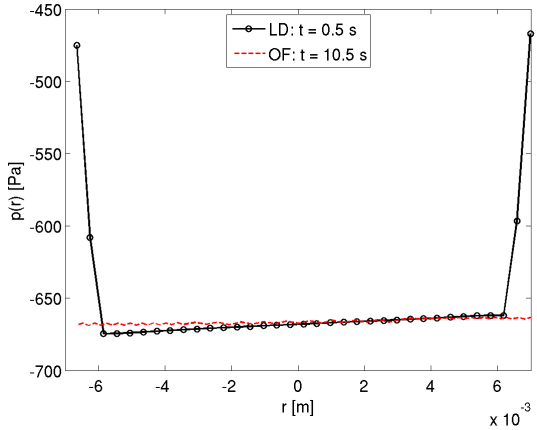

(d) Entrance pressure profiles

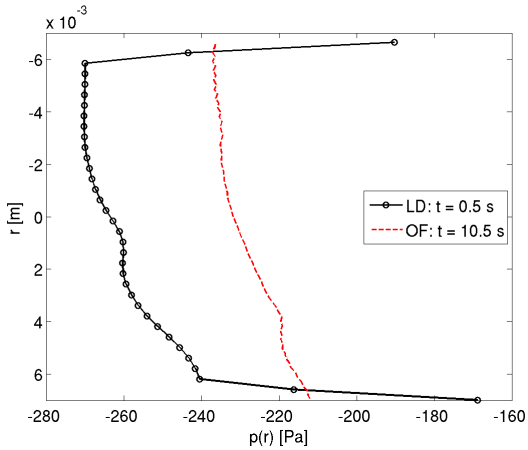

(e) Exit pressure profiles

Figure 4.8: Plots showing a) the stage of the inlet pulse, b,c) cross-section velocity profiles and d,e) cross-section pressure profiles at the entrance and exit of the bent EVG. Inlet velocity: $v_z = -0.5$ m/s.

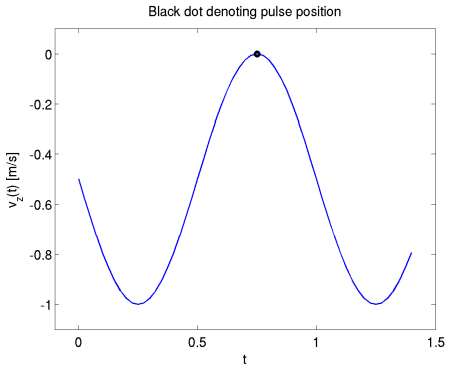

(a) Stage of inlet pulse (denoted by •)

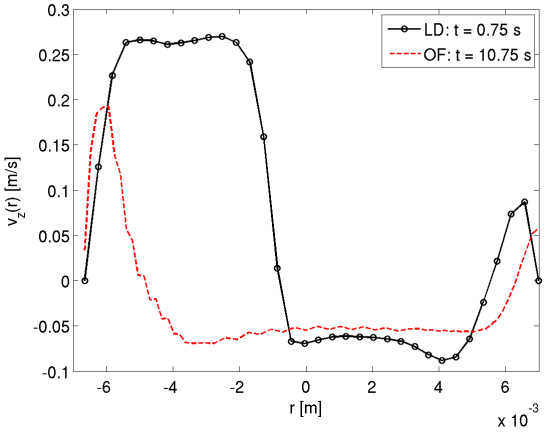

(b) Entrance velocity profiles

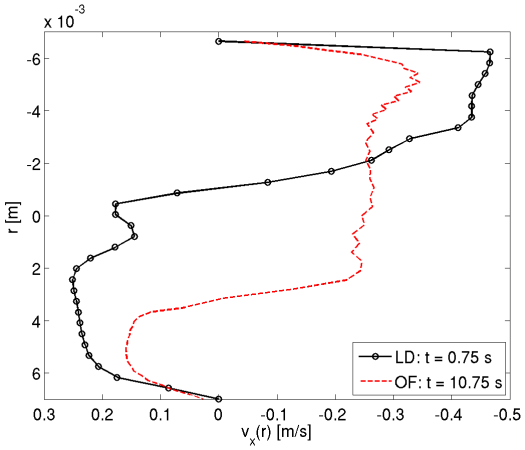

(c) Exit velocity profiles

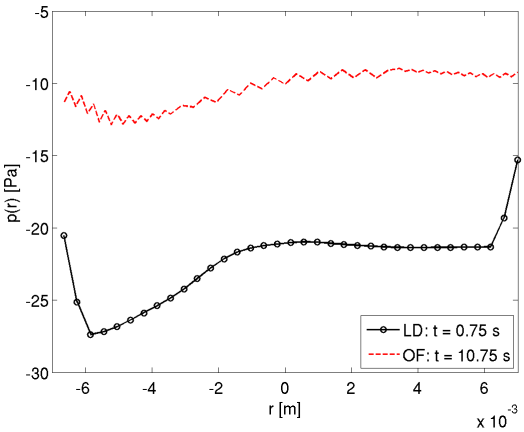

(d) Entrance pressure profiles

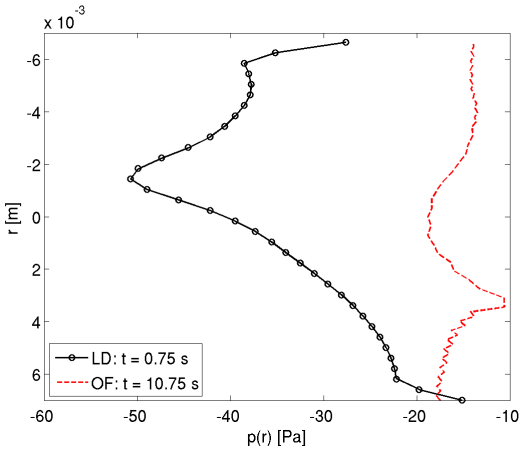

(e) Exit pressure profiles

Figure 4.9: Plots showing a) the stage of the inlet pulse, b,c) cross-section velocity profiles and d,e) cross-section pressure profiles at the entrance and exit of the bent EVG. Inlet velocity: $v_z = 0$ m/s.

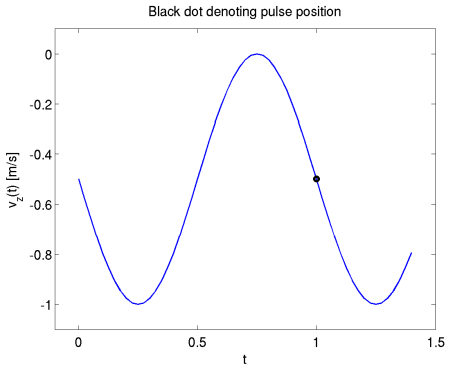

(a) Stage of inlet pulse (denoted by •)

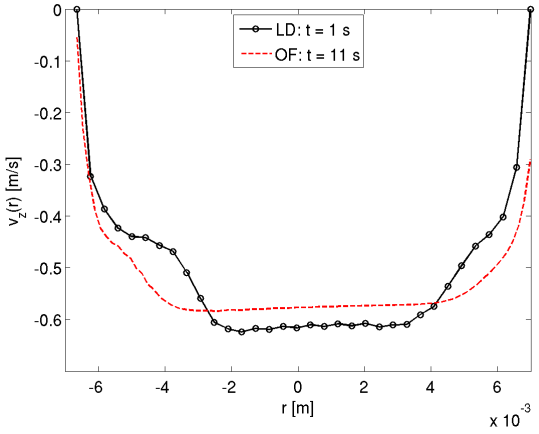

(b) Entrance velocity profiles

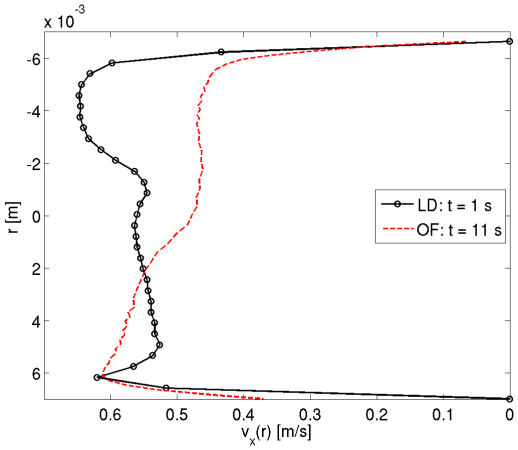

(c) Exit velocity profiles

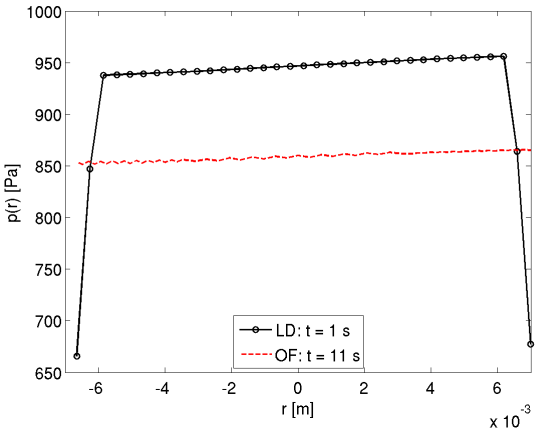

(d) Entrance pressure profiles

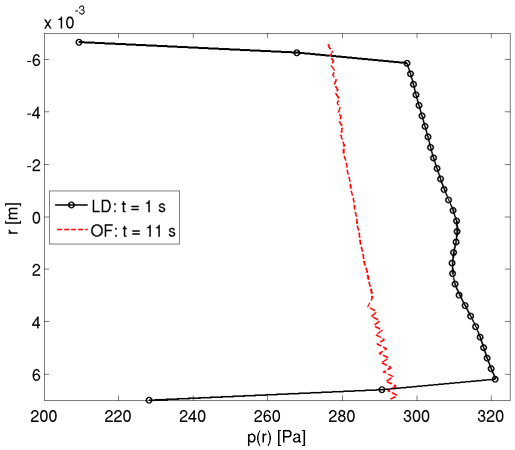

(e) Exit pressure profiles

Figure 4.10: Plots showing a) the stage of the inlet pulse, b,c) cross-section velocity profiles and d,e) cross-section pressure profiles at the entrance and exit of the bent EVG. Inlet velocity: $v_z = -0.5$ m/s.

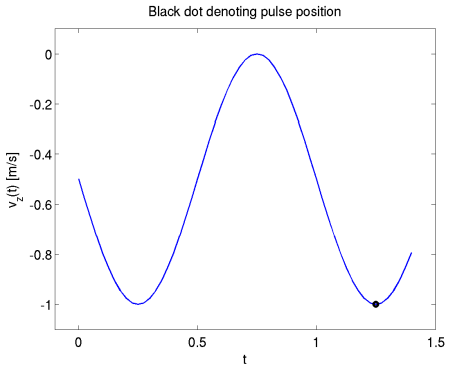

(a) Stage of inlet pulse (denoted by •)

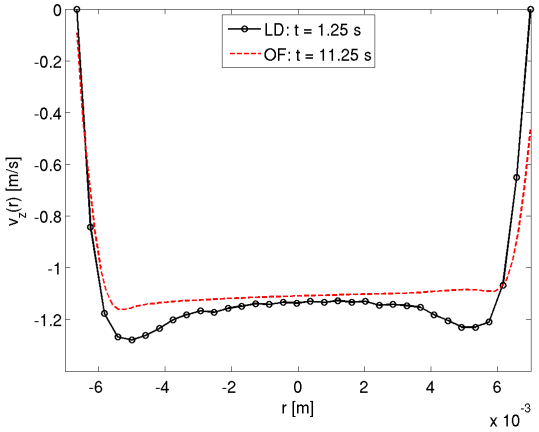

(b) Entrance velocity profiles

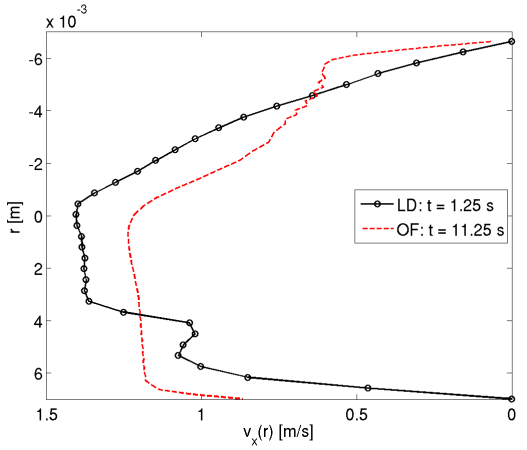

(c) Exit velocity profiles

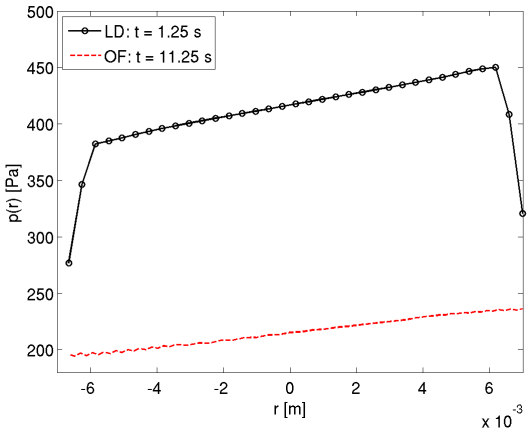

(d) Entrance pressure profiles

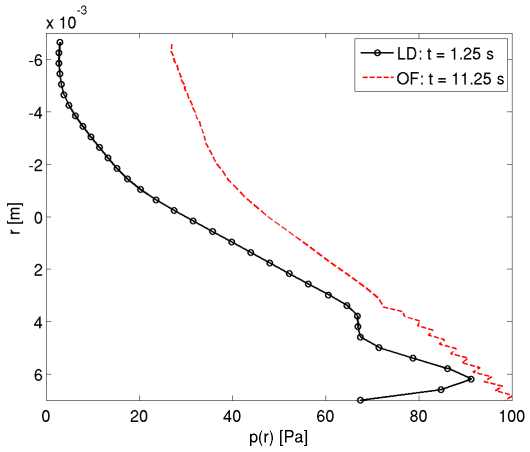

(e) Exit pressure profiles

Figure 4.11: Plots showing a) the stage of the inlet pulse, b,c) cross-section velocity profiles and d,e) cross-section pressure profiles at the entrance and exit of the bent EVG. Inlet velocity: $v_z = -1$ m/s.

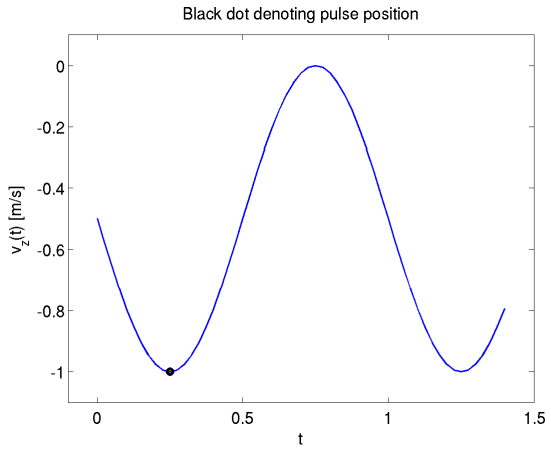

(a) Stage of inlet pulse (denoted by •)

Software	Upstream force [N]	Downstream force [N]
OF	0.1298	0.1058
LD	0.2286	0.1756

(b) Normal forces at current stage

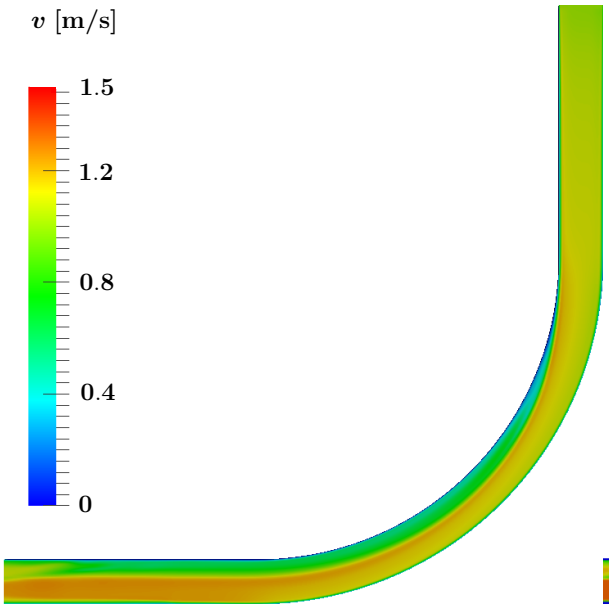

(c) Velocity field, OF

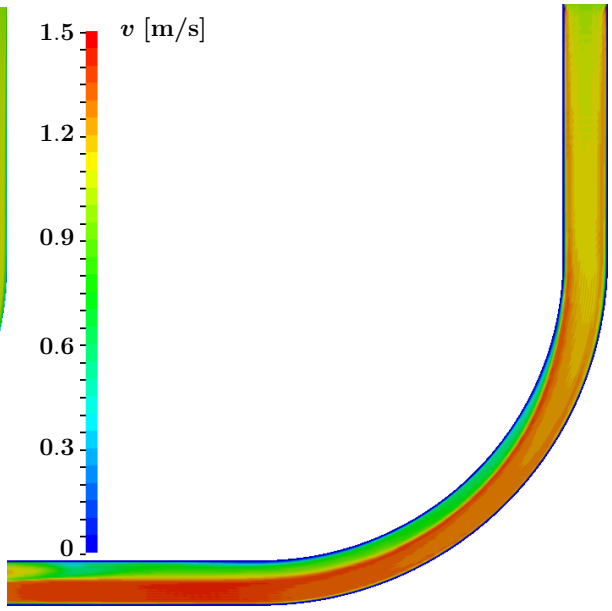

(d) Velocity field, LD

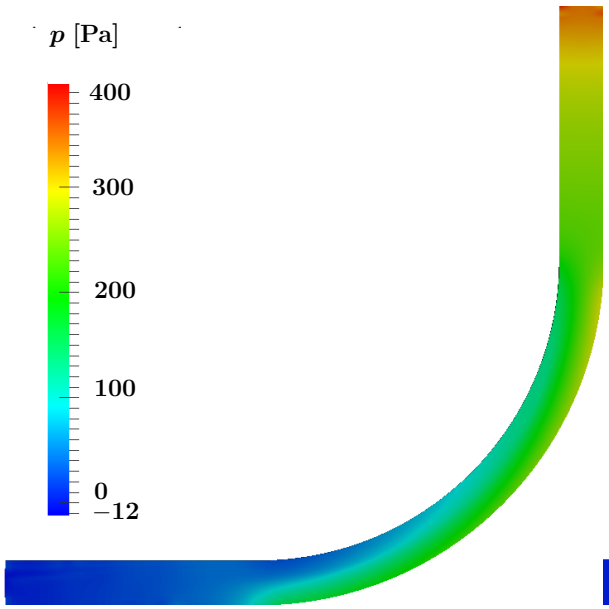

(e) Pressure field, OF

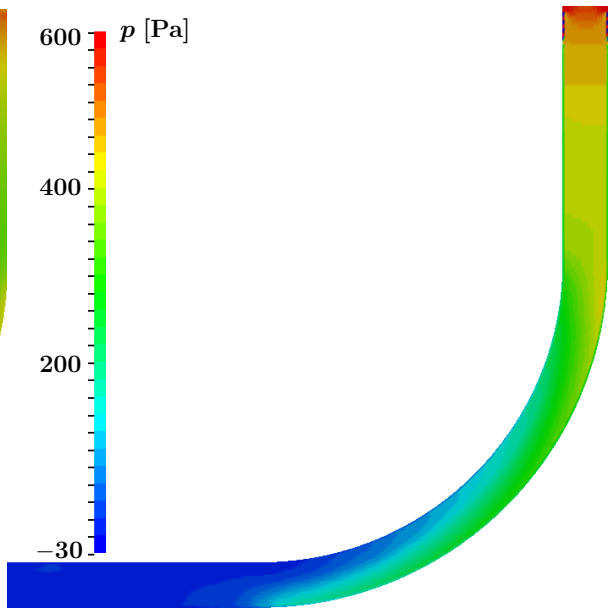

(f) Pressure field, LD

Figure 4.12: a) shows the stage of the inlet pulse, b) shows the normal forces at the current stage, c,d) show velocity fields from OF and LD, respectively, and e,f) show pressure fields from OF and LD, respectively.

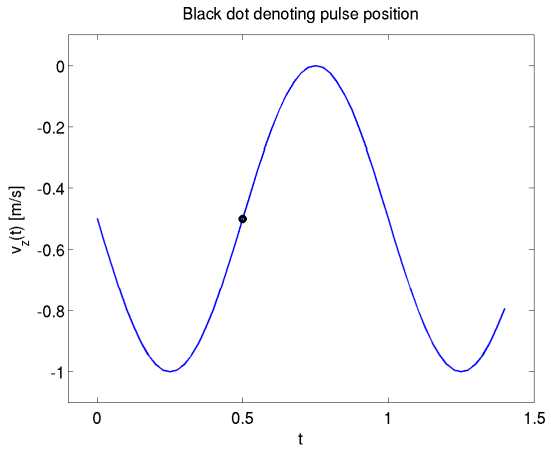

(a) Stage of inlet pulse (denoted by •)

Software	Upstream force [N]	Downstream force [N]
OF	-0.0644	-0.0721
LD	-0.0060	-0.0213

(b) Normal forces at current stage

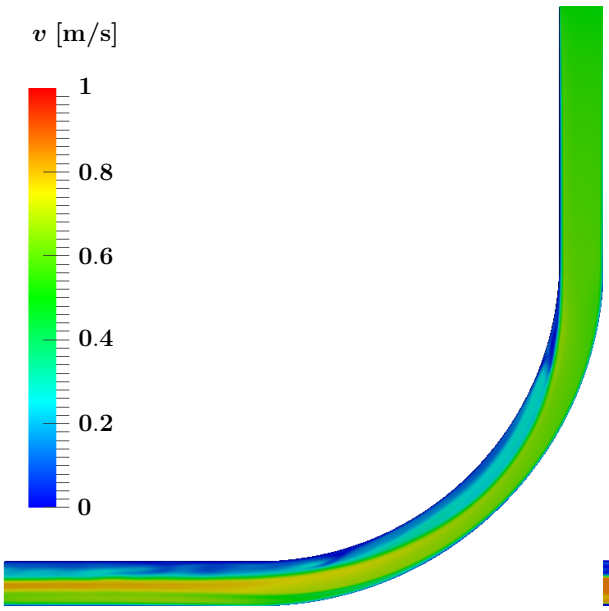

(c) Velocity field, OF

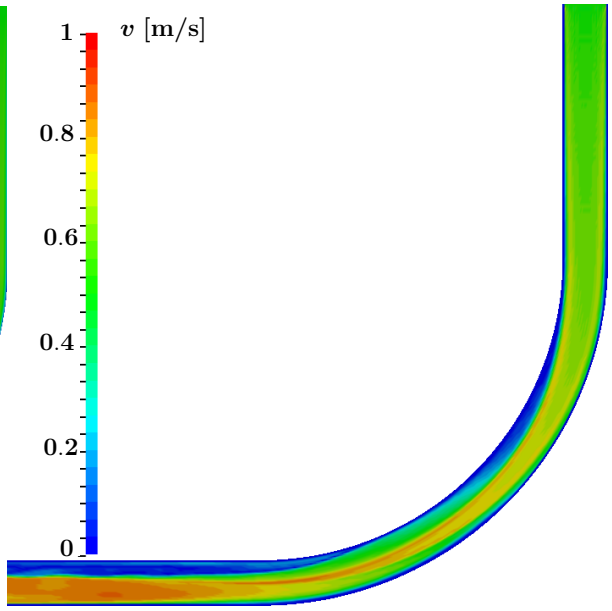

(d) Velocity field, LD

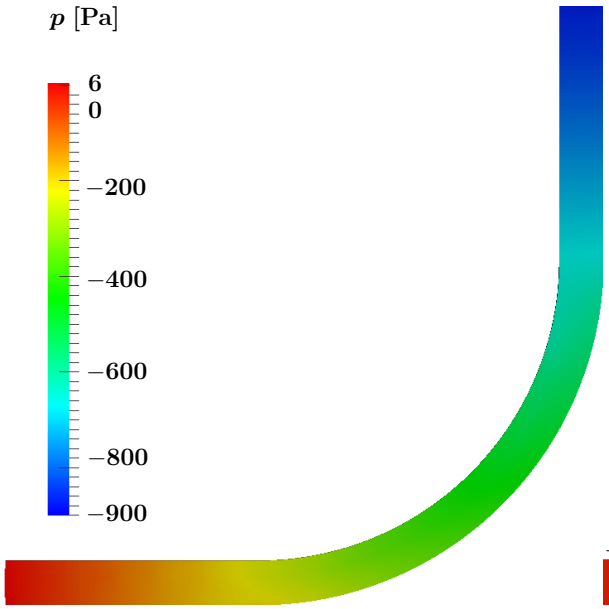

(e) Pressure field, OF

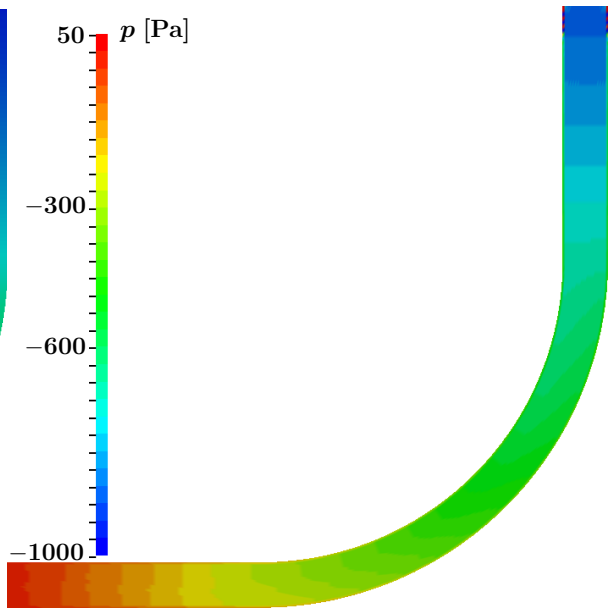

(f) Pressure field, LD

Figure 4.13: a) shows the stage of the inlet pulse, b) shows the normal forces at the current stage, c,d) show velocity fields from OF and LD, respectively, and e,f) show pressure fields from OF and LD, respectively.

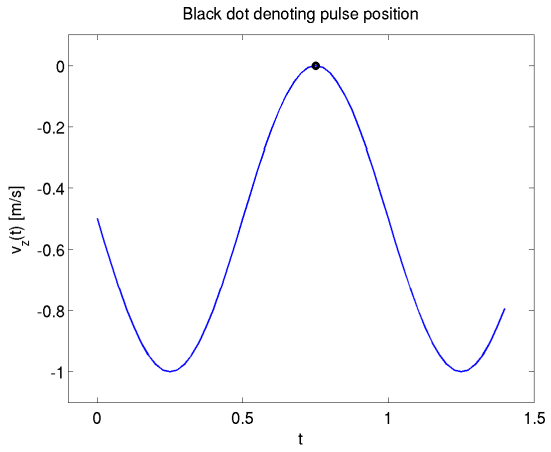

(a) Stage of inlet pulse (denoted by •)

Software	Upstream force [N]	Downstream force [N]
OF	-0.0420	-0.0452
LD	-0.0019	-3.6300e-04

(b) Normal forces at current stage

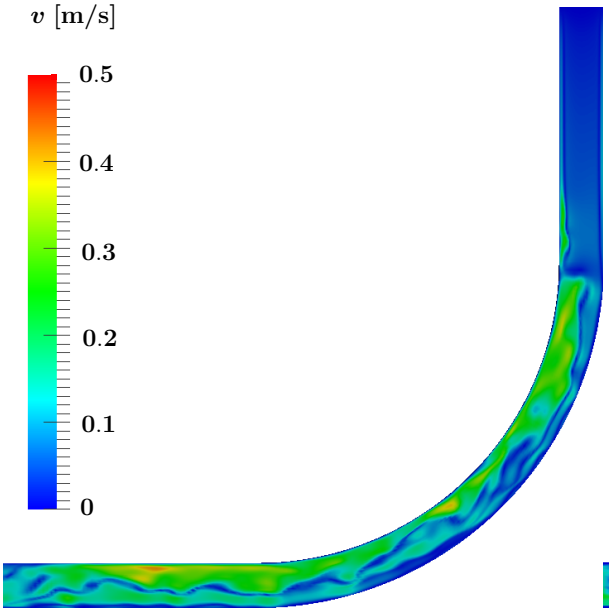

(c) Velocity fields, OF

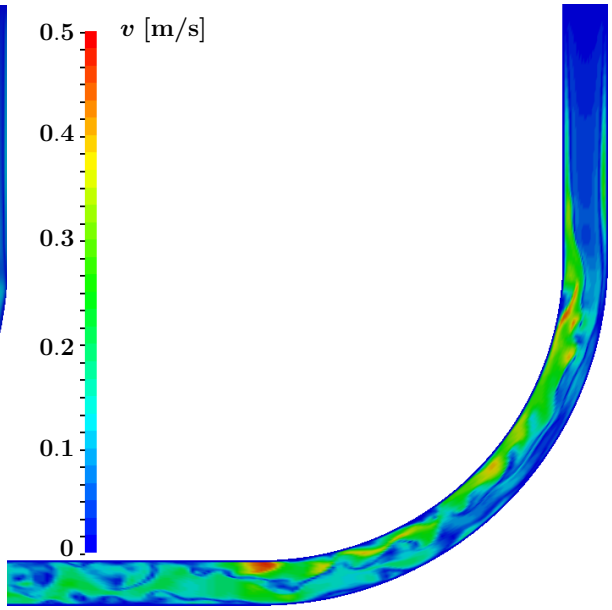

(d) Velocity fields, LD

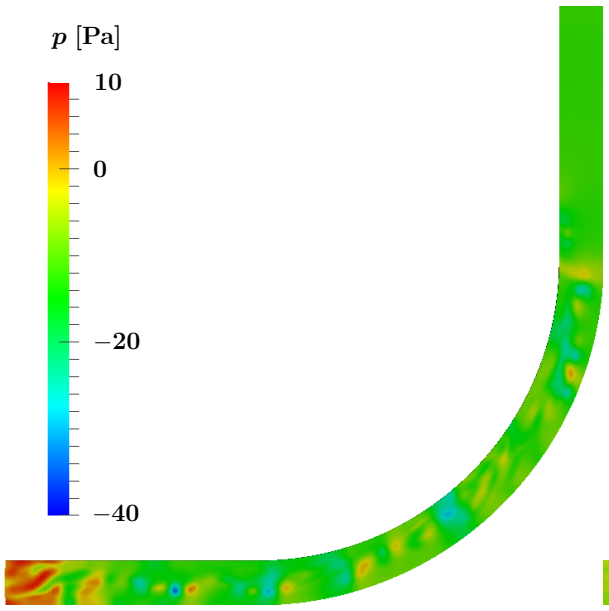

(e) Pressure fields, OF

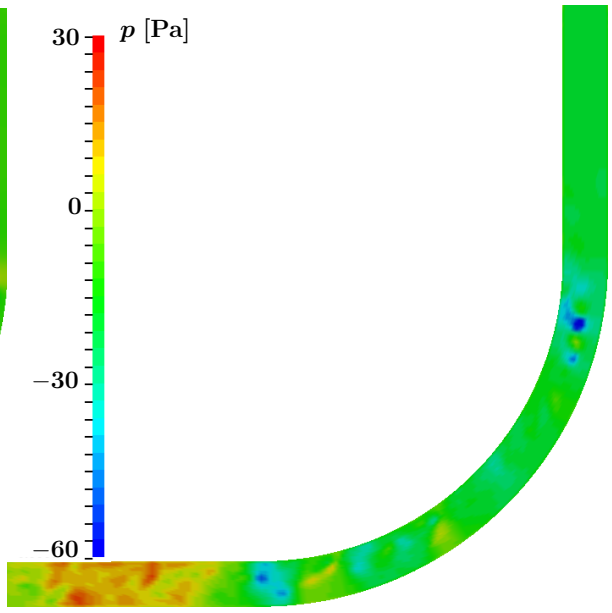

(f) Pressure fields, LD

Figure 4.14: a) shows the stage of the inlet pulse, b) shows the normal forces at the current stage, c,d) show velocity fields from OF and LD, respectively, and e,f) show pressure fields from OF and LD, respectively.

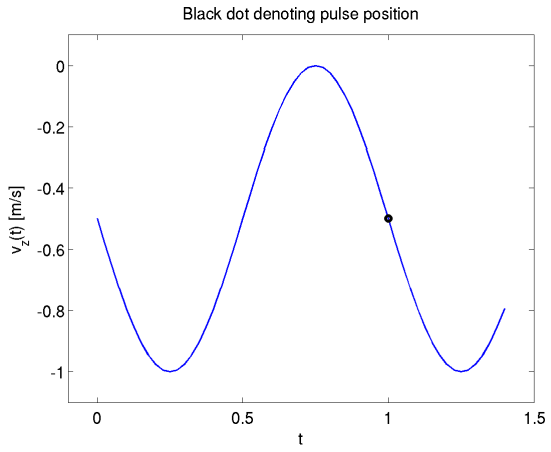

(a) Stage of inlet pulse (denoted by •)

Software	Upstream force [N]	Downstream force [N]
OF	0.0807	0.0639
LD	0.1441	0.1174

(b) Normal forces at current stage

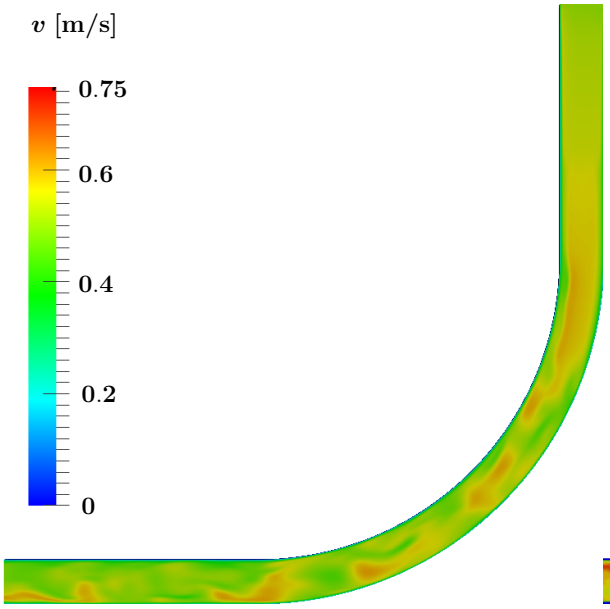

(c) Velocity fields, OF

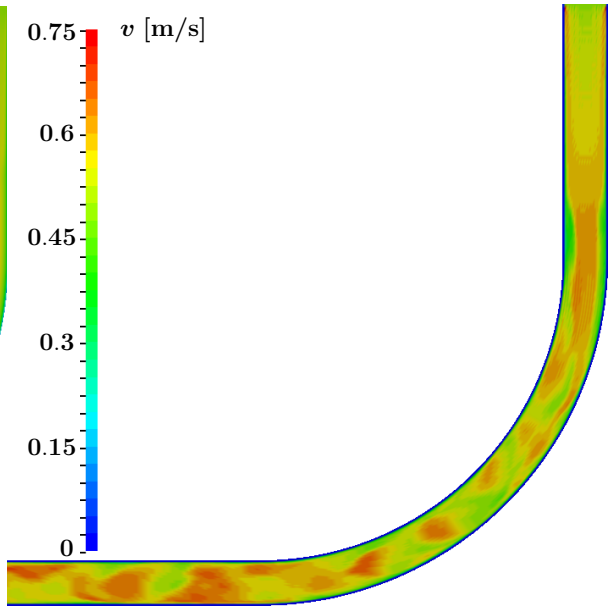

(d) Velocity fields, LD

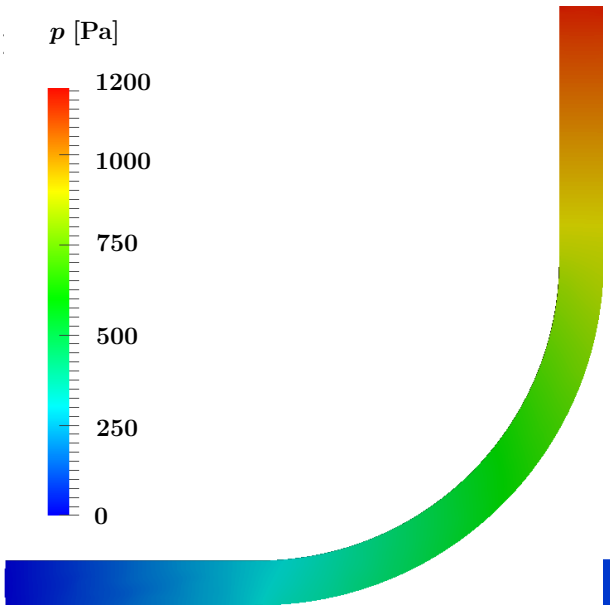

(e) Pressure fields, OF

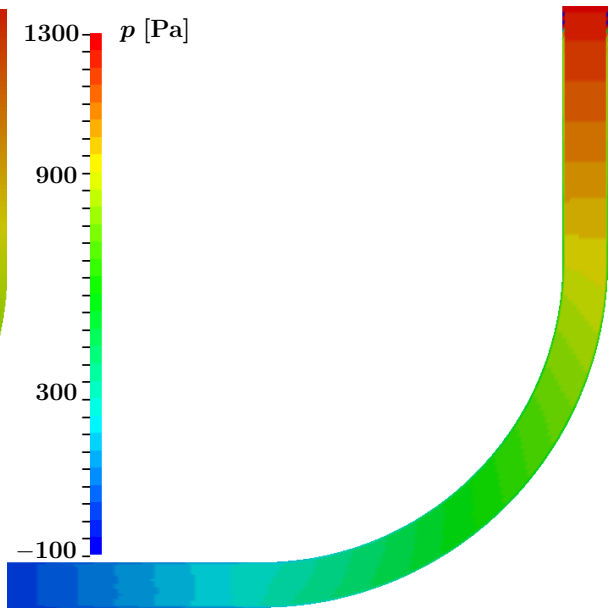

(f) Pressure fields, LD

Figure 4.15: a) shows the stage of the inlet pulse, b) shows the normal forces at the current stage, c,d) show velocity fields from OF and LD, respectively, and e,f) show pressure fields from OF and LD, respectively.

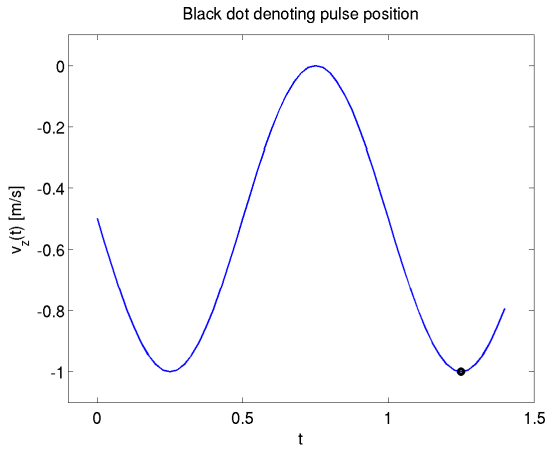

(a) Stage of inlet pulse (denoted by •)

Software	Upstream force [N]	Downstream force [N]
OF	0.1279	0.1039
LD	0.2278	0.1751

(b) Normal forces at current stage

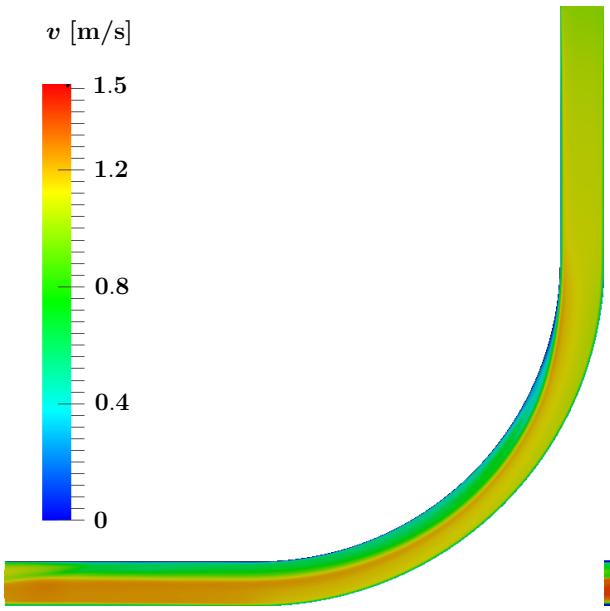

(c) Velocity fields, OF

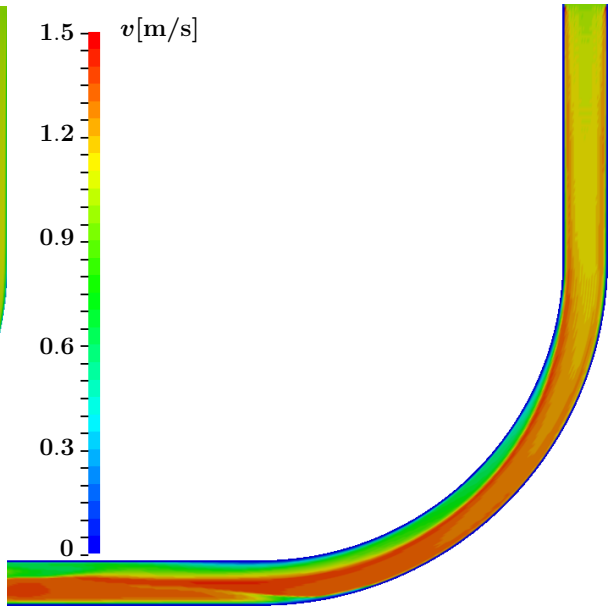

(d) Velocity fields, LD

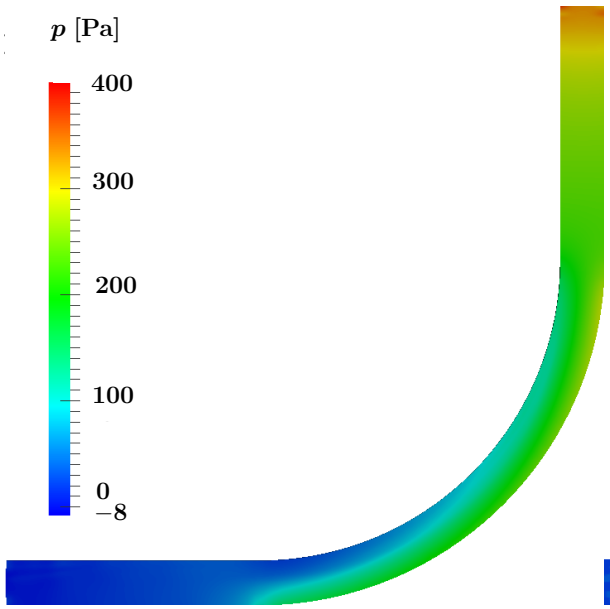

(e) Pressure fields, OF

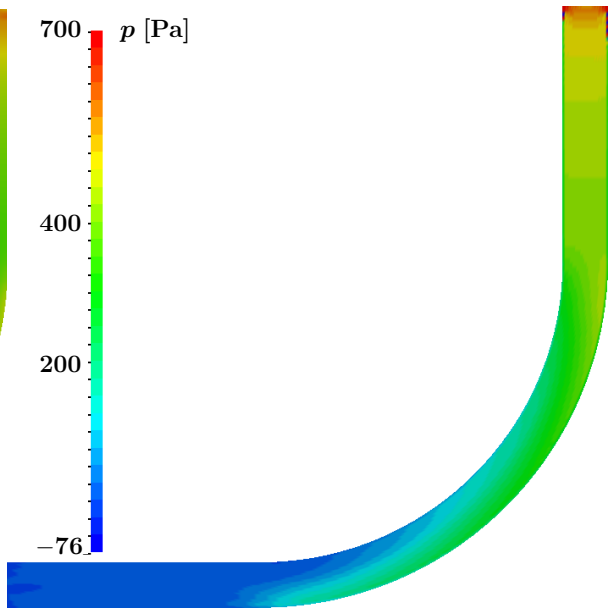

(f) Pressure fields, LD

Figure 4.16: a) shows the stage of the inlet pulse, b) shows the normal forces at the current stage, c,d) show velocity fields from OF and LD, respectively, and e,f) show pressure fields from OF and LD, respectively.

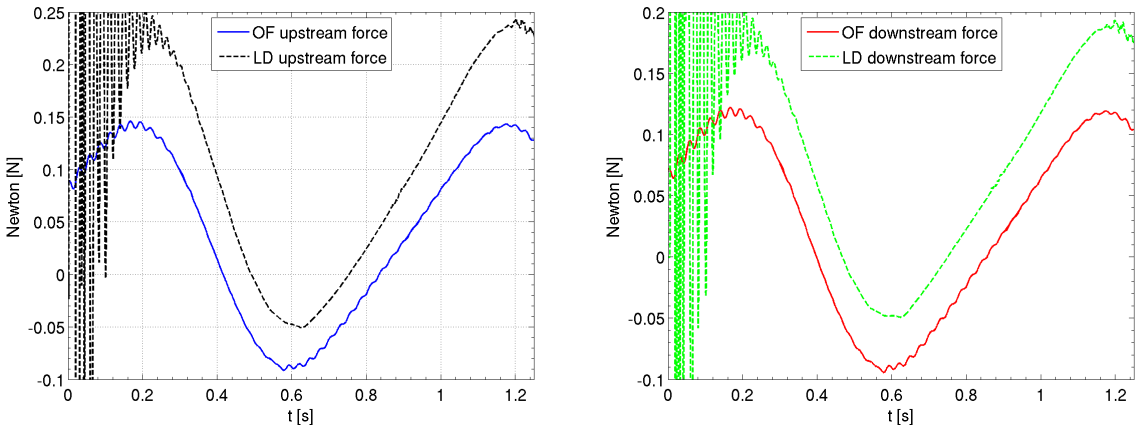

(a) Upstream normal forces (b) Downstream normal forces

Figure 4.17: Comparisons of upstream and downstream attachment normal forces for a sinusoidal inlet flow boundary condition.

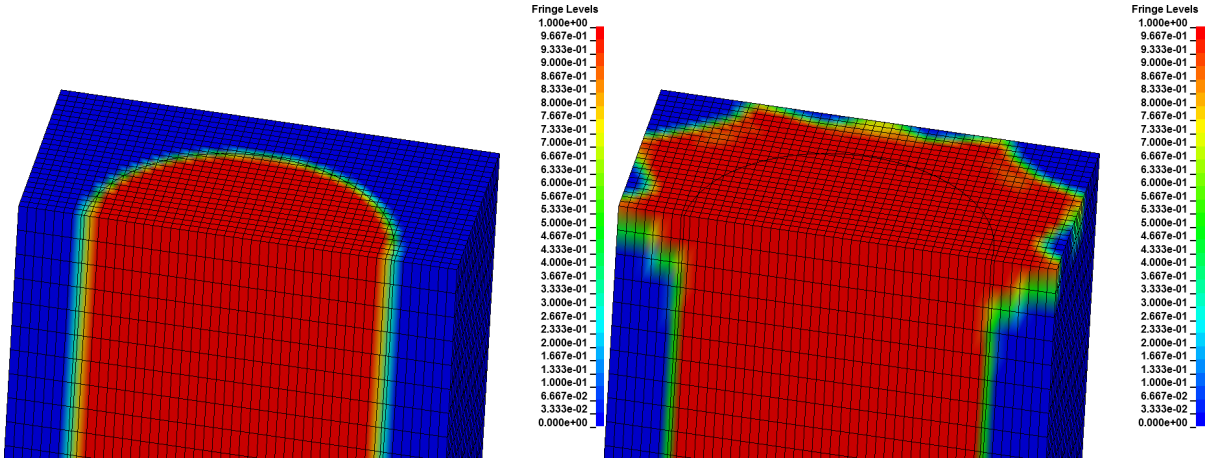

(a) Volume fraction $t = 0$ s (b) Volume fraction $t = 0.1$ s

Figure 4.18: a) showing initial volume fraction and b) the volume fraction after 0.1 s, illustrating the leakage for the pulsating flow case in LD.

5 Conclusions

As stated in Section 1.2, one of the main goals of this project is to investigate the possibility of using FSI simulations to assess the forces causing stent graft migration. Prior work, such as the ones performed by Li and Kleinstreuer [1, 24] and Molony et al. [25], demonstrate rather successful results from FSI simulations applying an FE approach and a mixed FE/FV approach, respectively. The force estimations in [1, 24] are the most relevant for comparison, since they are extracted at the bifurcating region of the EVG, and are in line with the forces estimated in the work by Malina et al. [5]. However, the forces extracted in the present study are inferior to the ones obtained by Li and Kleinstreuer. These differences most certainly originate from the dissimilarities in numerical approaches, boundary conditions, geometry and fluid medium. Furthermore, the forces are not extracted at the same locations.

Based on the work done by Li and Kleinstreuer [1, 24] and Molony et al. [25], the conclusion is that FSI simulations are realizable and possible to perform in such manner that a fair evaluation of the forces causing stent graft migration is achieved. However, this project does only offer results from further simplified simulations of the problem (see Section 1.4 and 1.5), also using different softwares than in prior studies. Nonetheless, the results show good promise of utilizing both LD and OF for more complex studies similar to those previously discussed. With this said, there are still several aspects that need to be improved and further tested to reach a more satisfactory level of complexity that further resembles an in vivo[5] stent graft. Examples of such improvements are a more aggressive (in terms of a steeper gradient), and hence more realistic, inlet pulse and a non-zero gauge pressure.

An additional purpose of this project is to compare the numerical approaches used in LD and OF. This is done by studying the velocity, pressure and resulting forces. Overall, LD gives higher magnitudes for these variables and this is mainly believed to be caused by the leakage of material and peaks in pressure and velocity at the inlet. Hence the credibility of these results is arguable. It is, however, likely that LD performs well with a finer tuned setup. For example, the constraint based coupling algorithm used in the present setup performs poorly for the rigid parts (i.e. the inlet and outlet) [26], though a penalty based coupling algorithm would instead require an extensive process of trial and error to establish important coupling parameters.

The approach used in OF does not suffer from any problems related to material mixing, since the different materials are separated into two different meshes. Instead, the largest difficulties are related to the remeshing procedure that follows a deformation of the structural mesh (and hence the displacement of the fluid-structure interface). The remeshing requirement leads to a sensitivity to large distortions, yielding an unstable and time consuming solution procedure (see Appendix D.2). Another drawback with the FV formulation is the requirement of volume elements, making it difficult to simulate very thin structures. On a more positive note, OF offers full insight to the source code, providing possibilities to investigate the implementation of the mathematical formulations and to implement modifications of the solver.

As a final remark, the authors believe that further testing and tuning of the modules used in this project can be of great interest, with the long-term objective of providing alternatives to the softwares used in prior studies. Since the setups used in this project partly lack complexity, it should be clearly stated that the forces extracted are not to be considered as guiding values in terms of in vivo stent graft migration. Nonetheless, the study provides helpful information about the functionalities of the two numerical approaches.

[5] i.e. within a living organism

6 Recommendations

As mentioned in Section 5, several improvements are to be considered for future studies. First and foremost, it is recommended to apply a more aggressive and realistic inlet pulse, similar to the ones used by e.g. Li and Kleinstreuer [1, 6, 24] and Molony et al. [25]. Additionally, a more representative gauge pressure is recommended in order to regard a larger inflation of the EVG, possibly contributing to larger forces. To gain further confidence in future studies it is recommended to perform parallel experimental and numerical studies, enabling comparisons of the results. Experimental studies may also be used to ensure proper material properties.

Furthermore, parametric studies of alternate geometries (e.g. EVG diameter and curvature) and alternate heart rates, possibly corresponding to patients suffering from hypertension[6], can be of great interest. In the long run it may also be meaningful to model a non-newtonian blood flow rather than water, since it impacts the flow behavior and hence the interaction with the EVG. Last, but not least, performing longer simulations would give the possibility to further investigate phenomenas such as the phase shift of forces in the pulsating case.

[6] i.e. elevated blood pressure

References

[1] Li, Z. & Kleinstreuer, C., "Analysis of biomechanical factors affecting stent-graft migration in an abdominal aortic aneurysm model," *Journal of Biomechanics*, vol. 39, 2006.

[2] Basford, J. R., "The Law of Laplace and Its Relevance to Contemporary Medicine and Rehabilitation," *Archives of Physical Medicine and Rehabilitation*, vol. 83, no. 8, 2002.

[3] Resch, T., Ivancev, K., Brunkwall, J., Nyman, U., Malina, M. & Lindblad, B., "Distal Migration of Stent-Grafts after Endovascular Repair of Abdominal Aortic Aneurysms," *Journal of Vascular and Interventional Radiology*, vol. 10, no. 3, 1999.

[4] Zarins, C. K., Bloch, D. A., Crabtree, T., Matsumoto, A. H., White, R. A. & Fogarty, T. J., "Stent graft migration after endovascular aneurysm repair: Importance of proximal fixation," *Journal of Vascular Surgery*, vol. 38, 2003.

[5] Malina, M., Lindblad, B., Ivancev, K., Lindh, M., Malina, H. & Brunkwall, J., "Endovascular AAA Exclusion: Will Stents With Hooks and Barbs Prevent Stent-Graft Migration?," *Journal of Endovascular Surgery*, vol. 5, no. 4, 1998.

[6] Li, Z. & Kleinstreuer, C., "Fluid-Structure Interaction Effects on Sac-Blood Pressure and Wall Stress in a Stented Aneurysm," *Journal of Biomechanical Engineering*, vol. 127, no. 4, 2005.

[7] Ponthot, J.P & Belytschko, T., "Arbitrary Lagrangian-Eulerian formulation for element-free Galerkin method," *Computer Methods in Applied Mechanics and Engineering*, vol. 152, 1998.

[8] Yeh, I., Chai, L. & Saha, N., "Application of ALE to airbag deployment simulation," *Int. J. Vehicle Safety*, vol. 1, no. 4, 2006.

[9] Toll, S. & Ekh, M., Lecture notes, "TME075 - Mechanics of solids & fluids. Part I: Fundamentals," August 2009.

[10] White, F. M., *Fluid Mechanics*. McGraw-Hill, 6th ed., 2008.

[11] Ottosen, N. & Petersson, H., *Introduction to the Finite Element Method*. Prentice Hall, 1st ed., 1992.

[12] Versteeg, H. K. & Malalasekera, W., *An Introduction to Computational Fluid Dynamics - The Finite Volume Method*. Prentice Hall, 2nd ed., 2007.

[13] Livermore Software Technology Corporation, *LS-DYNA Theory Manual*, 2006.

[14] Olovsson, L., Lecture notes, "LS-DYNA, Training class in ALE and fluid-structure interaction," May 2006.

[15] Kurose, S. & Takahashi, S., "Constraint-Based Simulation of Interactions Between Fluids and Unconstrained Rigid Bodies," in *Proceedings of the 2009 Spring Conference on Computer Graphics*, SCCG '09, ACM, 2009.

[16] Amsden, A. A., Ruppel, H. M., & Hirt, C. W., "SALE: A Simplified ALE Computer Program for Fluid Flow at All Speeds," Los Alamos Scientific Laboratory, 1980. LA-8095.

[17] Benson, D. J., "Momentum Advection on a Staggered Mesh," *Journal of Computational Physics*, vol. 100, no. 1, 1992.

[18] Tuković, Ž. & Jasak, H., "Updated Lagrangian Finite Volume Solver for large deformation dynamic response of elastic body," *Transactions of FAMENA*, vol. 31, 2007.

[19] Jasak, H & Weller, H. G., "Application of the finite volume method and unstructured meshes to linear elasticity," *International Journal for Numerical Methods in Engineering*, vol. 48, 2000.

[20] OpenCFD Limited, *OpenFOAM User Guide*, July 2009. version 1.6.

[21] Mörststedt, S-E. & Hellsten, G., *Data och Diagram - Energi- och kemitekniska tabeller*. Liber, 7th ed., 2008.

[22] Cutnell, J. D. & Johnson, K. W., *Physics*. Wiley, 4th ed., 1998.

[23] Graebel, W. P., *Engineering Fluid Mechanics*. Taylor & Francis, 1st ed., 2001.

[24] Li, Z. & Kleinstreuer, C., "Blood flow and structure interactions in a stented abdominal aortic aneurysm model," *Medical Engineering & Physics*, vol. 27, no. 5, 2005.

[25] Molony, D. S., Kavanagh, E. G., Madhavan, P., Walsh, M. T. & McGloughlin, T. M., "A Computational Study of the Magnitude and Direction of Migration Forces in Patient-specific Abdominal Aortic Aneurysm Stent-Grafts," *European Journal of Vascular and Endovascular Surgery*, vol. 40, no. 3, 2010.

[26] Livermore Software Technology Corporation, *LS-DYNA, Keyword User's Manual*, 2003.

A Analytical solution of laminar fully developed pipe flow

For a laminar, incompressible and fully developed flow through a straight circular pipe it is possible to find the exact solution of the Navier-Stokes equations. Considering a straight circular pipe of radius R, the governing equations can be rewritten in cylindrical coordinates by defining an arbitrary point P by a distance z along the central axis, a radial distance r from the central axis and a rotation angle θ about the same axis (cf. Figure A.1).

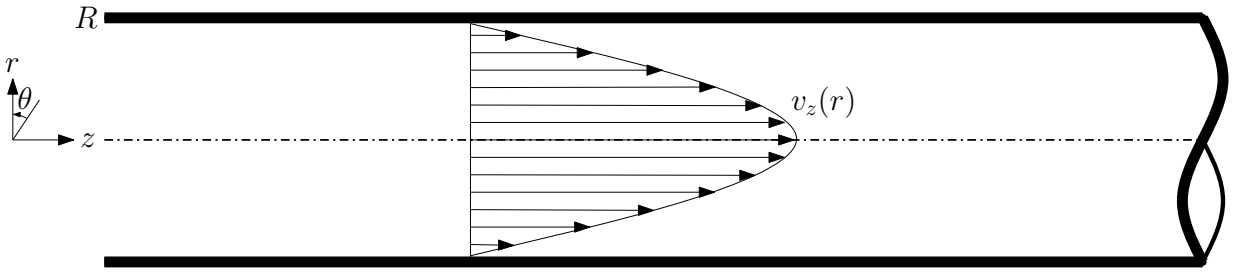

Figure A.1: A fully developed laminar velocity profile in a straight pipe.

The transformation from cartesian into cylindrical coordinates is governed by the following relations [10]:

$$r = \sqrt{x^2 + y^2}, \quad \theta = tan^{-1}\left(\frac{y}{x}\right), \quad z = z \tag{A.1}$$

Using (A.1) in equations (2.18) gives the Navier-Stokes equations in cylindrical coordinates:

$$r: \ \rho\left(\frac{\partial v_r}{\partial t} + v_r\frac{\partial v_r}{\partial r} + \frac{v_\theta}{r}\frac{\partial v_r}{\partial \theta} + v_z\frac{\partial v_r}{\partial z} - \frac{v_\theta^2}{r}\right) = -\frac{\partial p}{\partial r} + \mu\left[\frac{1}{r}\frac{\partial}{\partial r}\left(r\frac{\partial v_r}{\partial r}\right) + \frac{1}{r^2}\frac{\partial^2 v_r}{\partial \theta^2} + \frac{\partial^2 v_r}{\partial z^2} - \frac{v_r}{r^2} - \frac{2}{r^2}\frac{\partial v_\theta}{\partial \theta}\right] + \rho g_r \tag{A.2}$$

$$\theta: \ \rho\left(\frac{\partial v_\theta}{\partial t} + v_r\frac{\partial v_\theta}{\partial r} + \frac{v_\theta}{r}\frac{\partial v_\theta}{\partial \theta} + v_z\frac{\partial v_\theta}{\partial z} + \frac{v_r v_\theta}{r}\right) = -\frac{1}{r}\frac{\partial p}{\partial \theta} + \mu\left[\frac{1}{r}\frac{\partial}{\partial r}\left(r\frac{\partial v_\theta}{\partial r}\right) + \frac{1}{r^2}\frac{\partial^2 v_\theta}{\partial \theta^2} + \frac{\partial^2 v_\theta}{\partial z^2} + \frac{2}{r^2}\frac{\partial v_r}{\partial \theta} - \frac{v_\theta}{r^2}\right] + \rho g_\theta \tag{A.3}$$

$$z: \ \rho\left(\frac{\partial v_z}{\partial t} + v_r\frac{\partial v_z}{\partial r} + \frac{v_\theta}{r}\frac{\partial v_z}{\partial \theta} + v_z\frac{\partial v_z}{\partial z}\right) = -\frac{\partial p}{\partial z} + \mu\left[\frac{1}{r}\frac{\partial}{\partial r}\left(r\frac{\partial v_z}{\partial r}\right) + \frac{1}{r^2}\frac{\partial^2 v_z}{\partial \theta^2} + \frac{\partial^2 v_z}{\partial z^2}\right] + \rho g_z \tag{A.4}$$

The equation of continuity transformed into cylindrical coordinates reads

$$\frac{\partial \rho}{\partial t} + \frac{1}{r}\frac{\partial}{\partial r}\left(\rho r v_r\right) + \frac{1}{r}\frac{\partial\left(\rho v_\theta\right)}{\partial \theta} + \frac{\partial\left(\rho v_z\right)}{\partial z} = 0. \tag{A.5}$$

The concept *fully developed* means that the flow region studied is far enough from the pipe entrance to be considered purely axial, i.e. $v_z \neq 0$ and $v_\theta = v_r = 0$. By neglecting gravity and assuming axial symmetry (i.e. $\partial/\partial\theta = 0$), it then follows from (A.5) that

$$\frac{\partial v_z}{\partial z} = 0 \qquad \text{or} \qquad v_z = v_z(r) \qquad \text{only.} \tag{A.6}$$

This holds provided that the flow is steady and incompressible. Similarly, the r-momentum equation, eq. (A.2), simplifies to

$$\frac{\partial p}{\partial r} = 0 \qquad \text{or} \qquad p = p(z) \qquad \text{only.} \tag{A.7}$$

Consequently, equation (A.4) reduces to

$$-\frac{\partial p}{\partial z} + \frac{\mu}{r}\frac{\partial}{\partial r}\left(r\frac{\partial v_z}{\partial r}\right) = 0. \tag{A.8}$$

Equation (A.8) is linear and may be integrated twice yielding the result

$$v_z = \frac{\partial p}{\partial z}\frac{r^2}{4\mu} + C_1 \ln(r) + C_2 \tag{A.9}$$

where C_1 and C_2 are constants. The boundary conditions are no-slip at the wall and maximum velocity at the centerline (cf. Figure A.1):

$$\begin{aligned} r = 0; \qquad & \frac{\partial v_z}{\partial r} = 0 \\ r = R; \qquad & v_z = 0. \end{aligned} \tag{A.10}$$

The constants in equation (A.9) can then be obtained as

$$C_1 = 0 \qquad \text{and} \qquad C_2 = -\frac{\partial p}{\partial z}\left(\frac{R^2}{4\mu}\right). \tag{A.11}$$

The final expression for *laminar fully developed pipe flow* is now obtained as

$$\boxed{v_z(r) = -\frac{\partial p}{\partial z}\left(\frac{1}{4\mu}\right)\left(R^2 - r^2\right).} \tag{A.12}$$

B Simple force estimation for a steady flow

In order to establish confidence in the extracted forces, a simple calculation is performed to estimate the force needed to balance the change in momentum of an inviscid fluid as it is deflected in a bent streamtube (see Figure B.1a). Consider a fixed CV of a streamtube with the same steady, uniform inlet flow boundary condition and geometry as for the EVG (see Figure B.1b). The diameter $d = 0.014$ m yields a circular area of $A = \pi \cdot (d/2)^2$ m^2. Together with the density of water $\rho = 998$ kg/m^3 and the velocity

$$\mathbf{V}_{\text{In}} = [0\ 0\ -0.5], \quad \mathbf{V}_{\text{Out}} = [0.5\ 0\ 0] \quad \text{and} \quad |\mathbf{V}| = |\mathbf{V}_{\text{In}}| = |\mathbf{V}_{\text{Out}}| = 0.5 \text{ m/s}$$

yields a mass flow of

$$\dot{m} = \dot{m}_{\text{In}} = \dot{m}_{\text{Out}} = \rho A |\mathbf{V}| \approx 0.07682 \text{ kg/s}.$$

For a one dimensional cross section, where $\mathbf{V}$ and ρ is uniform over the area and with the conservation of mass, the linear momentum equation reads [10]

$$\mathbf{F} = \frac{\mathrm{d}}{\mathrm{d}t}\left(\int_{CV} \mathbf{V}\rho \, \mathrm{d}V\right) + (\dot{m}\mathbf{V})_{\text{Out}} - (\dot{m}\mathbf{V})_{\text{In}} \tag{B.1}$$

The volume integral vanishes for a steady flow, such that the force becomes

$$\mathbf{F} = \dot{m}(\mathbf{V}_{\text{Out}} - \mathbf{V}_{\text{In}}). \tag{B.2}$$

This yields the x and y force components

$$F_x = F_z \approx 0.03841 \text{ N}.$$

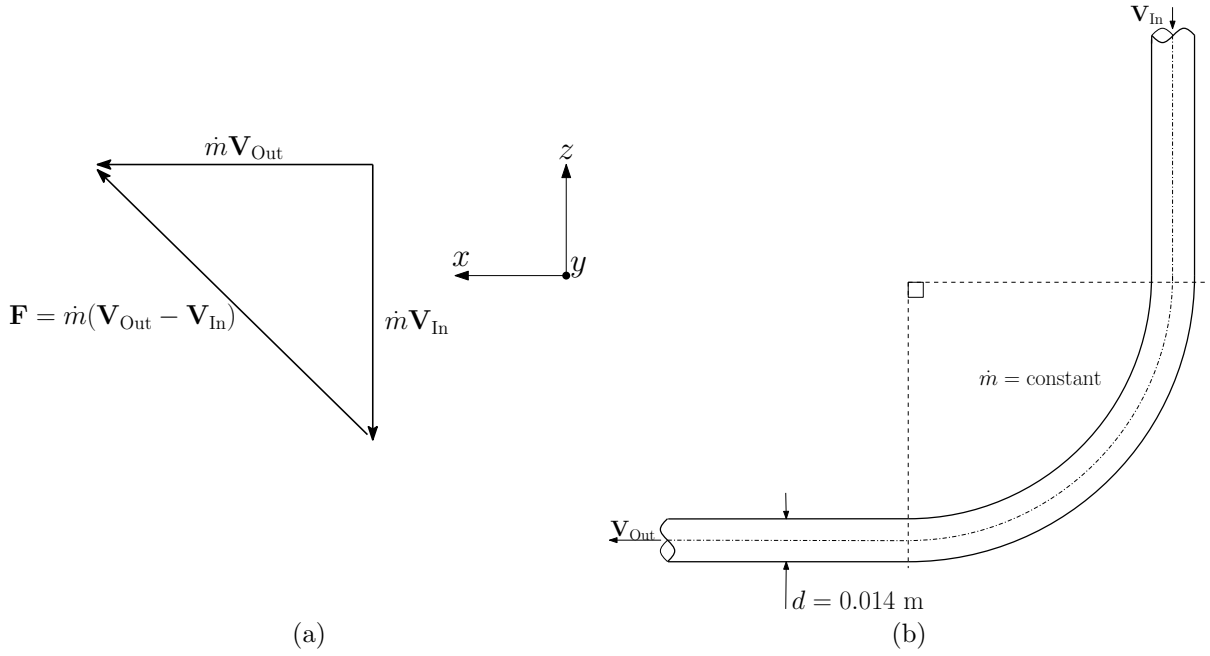

Figure B.1: a) shows a vector diagram for force calculation and b) a streamtube in steady flow.

C LS-DYNA implementation

The ALE method in LS-DYNA demands several important input cards in order to get a correct case setup (see Table C.1 below). This section presents the used cards and offers some explanation regarding their function. The reader is recommended to only read this text as a complement to the LS-DYNA manual.

Table C.1: Important input cards in the LS-DYNA setup

Input card name	
*CONTROL_ALE	Card to define for example number of advection cycles and whether or not mesh smoothing should be performed
*CONTROL_TERMINATION	Set termination time.
*CONTROL_TIMESTEP	Contains parameters for timestep control
*CNSTRND_LAGRANGE_IN_SOLID	Card to define Lagrangian and Eulerian coupling. Coupling can either be of penalty or constrained type (cf. section 2.4.3). If penalty method, parameters such as damping and penalty factor can be set.
*ALE_MULTI-MATERIAL_GROUP	Card used to associate material, defined via part, with its respective volume fraction, referred to as AMMG.
*INITIAL_VOLUME_FRACTION_GEOMETRY	Initializes the volume fraction constrained by selected container geometry. Here the AMMG-cards are configured to fill within the set container or to be the background material.
*MAT_ALE_VISCOUS	Defines the viscous material given the properties of chosen fluid. Demands an equation of state card (see below).
*MAT_ALE_VACUUM	Material card for defining "dummy" material for non computational fluid domain.
*EOS_LINEAR_POLYNOMIAL	Used to define the bulk viscosity by only setting C1 equal to value of choice.
*DBASE_NODAL_FORCE_GROUP	Group card to define from which nodes to collect the nodal forces. Output controlled from ASCII_option card.
*SOLID_ALE	Card to set element formulation options, associated with Eulerian part in their respective part card.

D OpenFOAM implementation

As mentioned in Section 2.5 the simulation in OpenFOAM was performed using an extended version of the `icoFsiFoam` solver. This section covers the case setup, as well as the steps which the FSI simulations are divided into.

D.1 Case setup

The file structure for cases run with this solver differs somewhat from the typical standard (single-phase) cases in OpenFOAM. First off, the case is divided into two separate subfolders; one for the fluid simulation and one for the structural simulation. These folders are, from now on, referred to as `fluid` and `solid`, respectively. The file structures for the `fluid` and `solid` directories look as follows:

```
fluid                                    solid
|-- 0                                    |-- 0
|   |-- motionU                          |   `-- DU
|   |-- p                                |-- constant
|   |-- solid -> ../../solid/0           |   |-- polyMesh
|   `-- U                                |   |   |-- boundary
|-- constant                             |   |   |-- cellZones
|   |-- couplingProperties               |   |   |-- faces
|   |-- dynamicMeshDict                  |   |   |-- faceZones
|   |-- polyMesh                         |   |   |-- neighbour
|   |   |-- boundary                     |   |   |-- owner
|   |   |-- cellZones                    |   |   |-- points
|   |   |-- faces                        |   |   |-- pointZones
|   |   |-- faceZones                    |   |   |-- sets
|   |   |-- neighbour                    |   |   |   `-- interfaceSolidZone
|   |   |-- owner                        |   |   `-- zoneToPatchName
|   |   |-- points                       |   `-- rheologyProperties
|   |   |-- pointZones                   |-- system
|   |   |-- sets                         |   |-- controlDict
|   |   |   `-- interfaceFluidZone       |   |-- decomposeParDict
|   |   `-- zoneToPatchName              |   |-- fvSchemes
|   |-- solid -> ../../solid/constant    |   |-- fvSolution
|   `-- transportProperties
|-- system
|   |-- controlDict
|   |-- decomposeParDict
|   |-- fvSchemes
|   |-- fvSolution
|   |-- sampleDict
|   |-- solid -> ../../solid/system
|   `-- tetFemSolution
```

The initial and boundary conditions are defined in the `0` directories located directly under the `fluid` and `solid` directories. The pressure and velocity conditions for the fluid are defined in `p` and `U`, respectively, while the displacement increment condition for the

structure is defined in `DU`. The file `motionU` contains the conditions for the deforming mesh motion, which is a requirement for the FSI analysis. The motion of the mesh at the fluid-structure interface has to be implemented as a Dirichlet boundary condition for the fluid velocity. This is done using `movingWallVelocity` as the boundary condition in `U` at the interface.The `constant` subdirectories (i.e. `polyMesh`, `transportProperties` and `rheologyProperties`) contain information about the meshes and the material properties (e.g. density, viscosity, Young's modulus etc.) for the different phases. Most of the settings governing the fluid-structure interaction are defined in `couplingProperties` and the settings for the solution of the mesh motion are defined in `dynamicMeshDict`. The `system` directories are where the solution procedure is setup. Settings such as end time, time step and time interval for output to be written are all defined in the file `controlDict`. The files `fvSchemes` and `fvSolution` contain information about which differencing schemes to use and settings for convergence tolerances. The `decomposeParDict`s describe how the computational domains should be decomposed for cases that are to be run in parallel. The branches of the type `solid ->` are, so-called, soft links linking together the settings for the fluid phase with the solid phase. These links are necessary in order for the solver to get input to the solution of both the fluid and structural equation systems.

The fluid-structure interface is defined after the fluid and solid meshes have both been created. This is done by typing

```
setSet -case fluid

faceSet <fluidInterfaceName> new patchToFace <fluidInterfacePatchName>

quit

setsToZones -case fluid -noFlipMap

setSet -case solid

faceSet <solidInterfaceName> new patchToFace <solidInterfacePatchName>

quit

setsToZones -case solid -noFlipMap
```

when standing in the main case folder. The interface could then be used for the settings in the file `couplingProperties` located in the subdirectory `fluid/constant`. This file contained the residual tolerance for the FSI.

Since the straight pipe in the first study (see Section 3.2) are to be given rigid walls, the coupling implementation of the solver has to be turned off, making it solve only for the flow. This is done by setting

```
fsi     no;
```

in `couplingProperties`.

D.2 Simulation steps

Due to convergence problems, the OF FSI simulations have to be split into three stages. They are

1. Perform an initial, uncoupled steady flow simulation. Run until stabilized.
2. Perform an uncoupled, pulsating flow simulation. Run for a few pulses.
3. Perform a coupled, pulsating flow simulation.
    i) Calculate normal forces in EVG attachments.

Thanks to this procedure, large initial instabilites (which causes the solution to diverge) can be avoided.